

Deformation and geomorphology at intermediate time scales

9

Studies of tectonic geomorphology at intermediate time scales provide opportunities to gather a different suite of insights on both tectonic deformation and landscape responses than can be obtained from investigations confined to the Holocene. By “intermediate” time scales, we refer to intervals extending from the Holocene–Pleistocene boundary at 11.6 ka (Steffensen *et al.*, 2008) to about 300–400 ka. Over such time scales, the landscape becomes a summation of both episodic and continuous tectonic and geomorphic processes. Whereas many active faults will have experienced only a few earthquakes during the Holocene, these faults may sustain dozens to hundreds of earthquakes over 300 000 years. These repetitive ruptures smooth the variations in displacements that frequently occur between any two successive earthquakes (Fig. 4.4), such as might be seen during the Holocene, and they cumulatively allow better, more confident definition of long-term mean rates of deformation.

Knowledge of such longer-term rates is invaluable when trying either to understand the implications of a shorter-term record or to assess its relevance to other time scales. For example, geodetic measurements collected over a few years are now being used by a growing number of researchers to characterize long-term rates of regional deformation. But, are the rates measured at decadal scales truly typical of tectonic rates over 100 000 years or more

(Fig. 5.1)? Only knowledge of rates at these longer time scales can answer that question. Similarly, the persistence of deformation rates and calculated recurrence intervals based on trenching studies of Holocene faulting can only be assessed using a longer-term record. Thus, by considering intermediate time scales, more representative averages can be obtained for deformation rates.

At time scales of more than 10 kyr, erosion becomes an increasingly important factor in modifying the landscape. Pristine tectonic forms become degraded over these longer intervals. Sufficient time elapses for interactions between discrete deformation events and ongoing surface processes to shape the landscape into characteristic forms, such that river patterns, dissected limbs of folds, and modified fault scarps can be viewed as recording these interactions. At time scales extending well beyond the Holocene, interpretation of the stratigraphic record becomes increasingly important as an approach to reconstructing past deformation: as mountains are eroded, their history can be recorded by the sediments eroded from them. Fortunately, at intermediate time scales, many tectonically produced topographic features are still sufficiently well preserved that they provide clear evidence of the summation of individual tectonic events that determined their shape.

At scales of hundreds of millenia, intermediate time scales smooth the intrinsic variability of

weather and provide a better long-term average of the fluxes of water, temperature, and winds that drive most surface processes. Superimposed on any such average conditions, however, are major glacial-interglacial cycles that create a strong, complex, and highly variable climate signal, which, in turn, modulates surface processes as they shape the landscape. Across such cycles, we should expect: (i) sea level to fluctuate by more than 100 m; (ii) major changes in sediment fluxes, discharge, and erosive capacity in rivers; and (iii) variations in hillslope stability as moisture content, soils, vegetation, and hillslope diffusivities change in response to climate. All such changes commonly complicate the interpretation of the landscape.

Despite the geomorphic changes wrought by changing climate, such climatic forcing also creates additional evidence in the landscape that allows better determination of the tectonic rates and processes. Geomorphic markers, such as marine or fluvial terraces, which form in response to climatic variability, can provide multiple reference surfaces with which to define the geometry of deformation. If the ages of these markers can be determined, then intermediate-term rates of deformation can be calculated. At these time scales, it is sometimes also possible to distinguish between the climatic and the tectonic imprint on the landscape. Consider the growth of a simple fault-bend fold. At the scale of individual seismic events, its growth is highly episodic, such that instantaneous spurts of growth are followed by extended quiescent intervals. Over the span of numerous faulting events, however, the fold will be seen to grow continuously. In contrast, climatically controlled processes will typically be relatively steady at the scale of a single or a few seismic events, whereas they become highly variable at those intermediate time scales over which tectonic processes may appear steady. Such contrasts between the time scales of episodicity and steadiness in tectonic versus climatic processes provide an excellent opportunity to try to separate their relative influence on both evolving landforms and sedimentary successions related to those landforms. Given a desire to understand how tectonically influenced landscapes evolve

through time or to reconstruct depositional or erosional responses that are likely to be preserved in the stratigraphic record, this more time-averaged landscape offers an important geological perspective.

Unresolved problems at intermediate time scales

Certain classes of problems are best attacked at intermediate time scales – those in which the signals of interest need to be integrated across many millennia. Most commonly, those same signals need to record significant change at these same time scales. For example, when snapshots of a fault or landscape can be captured at multiple moments over many tens to hundreds of millennia, diverse models for fault behavior and landscape evolution can be tested. Because faults commonly grow at time scales of 10^4 – 10^6 years, observations of well-dated geomorphic markers can enable us to test competing models for fault growth. For example, do faults obey the classic concept of progressive lengthening with each successive earthquake? Or, do they rapidly achieve an approximately fixed length early in their history if they encounter barriers that restrain their tips (Fig. 9.1)? The latter model predicts faults dominated by “characteristic earthquakes” (Fig. 4.7), whereas the former model predicts continuous change in fault length with time. These models can be tested if data are available over sufficiently long time intervals (many millennia), because both the position of successive fault tips and the shape of the displacement profiles change with time in distinctive ways for each model.

Climatic changes at intermediate time scales have clearly led to the waxing and waning of glaciers, as well as to the growth and shrinkage of lakes. Because both expanding glaciers and lakes impose new loads on the crust, we might wonder whether their growth and decay could influence the behavior of faults. If changes in the balance between maximum and minimum stresses on fault surfaces were sufficiently great, then rates of fault slip might be expected to vary in concert with the climatically induced changes in crustal loads (Fig. 9.2). In fact, depending on

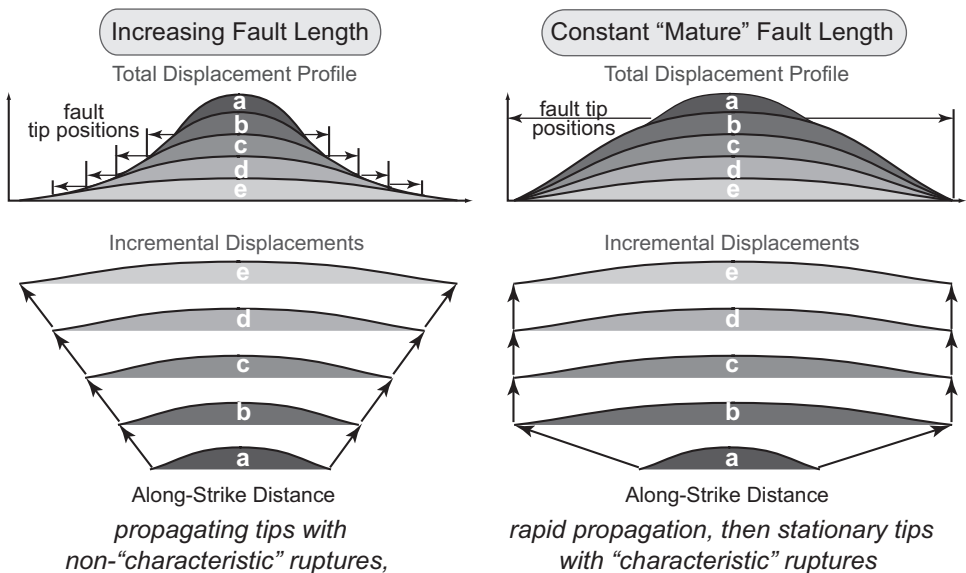


Fig. 9.1 Competing models for accumulation of displacement on faults.

(Left) The “traditional” model suggests faults lengthen in each rupture as they accumulate displacement. (Right) The “fixed length” model suggests that faults propagate rapidly in early stages of growth, stop lengthening as fault tips encounter strong barriers, and then simply accumulate displacement at a nearly fixed length. Modified after Amos *et al.* (2010).

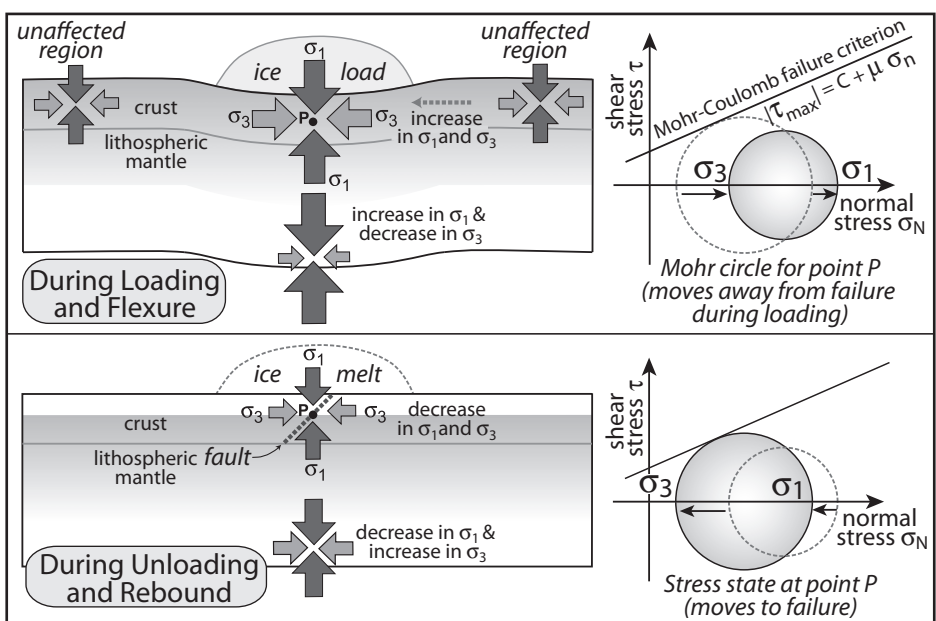


Fig. 9.2 Conceptual linkages between crustal loads and fault slip.

Suppression of fault slip during temporary loading by glaciers or lakes. (Top) Ice (or water) loads and associated crustal flexure can increase crustal stresses such that a fault is moved farther away from failure (as represented by the Mohr-Coulomb failure criterion). (Bottom) Removal of the load and crustal rebound can then drive the fault to the point of failure. Modified after Hampel and Hetzel (2006).

the sensitivity of faults to small changes in loads, spatial and temporal changes in the locus and/or rates of bedrock erosion in a mountain belt due to climate variability might also modulate fault slip rates. Given the striking correlation of seasonal cycles of monsoon-modulated water loads in the Himalayan foreland (see Box 5.2) with both Himalayan seismicity and convergence rates (Bettinelli *et al.*, 2008), these proposed linkages between climate and fault slip rates at intermediate time scales make conceptual sense. Nonetheless, more high-resolution data are needed at these time scales to explore the characteristics of such potential linkages.

Because plate convergence rates can be as high as 100 km/Myr, unsteadiness in convergent processes should be well expressed at intermediate times scales. For example, geomorphic studies along subduction zones have shown that, when seamounts or a rough sea floor impinge on a trench, the forearc deforms (Fisher *et al.*, 1998). But, can the timing, wavelength, and magnitude of that deformation provide insight into the tectonic processes and kinematics that govern the collision? Again, competing models (Taylor *et al.*, 2005) make contrasting predictions for the pattern and rates of deformation at intermediate time scales (Fig. 9.3). If a seamount that is rafted along by a subducting plate steadily slips beneath the forearc, it should generate a migrating wave of forearc uplift and subsidence at spatial and temporal wavelengths that scale with the size of the seamount and the convergence rate. In contrast, if the seamount gets stuck against the forearc, collisional stresses could be abruptly transferred to the outer forearc and might drive rapid uplift above a subduction zone that had become temporarily locked. If the plate interface eventually ruptures through the seamount, the release of those stresses could drive rapid subsidence. These different forearc behaviors can be assessed with data gathered at intermediate time scales.

In this chapter, two different aspects of tectonic geomorphology at intermediate time scales will be examined. First, techniques for calibration of rates of deformation are illustrated by focusing on the use of various types of

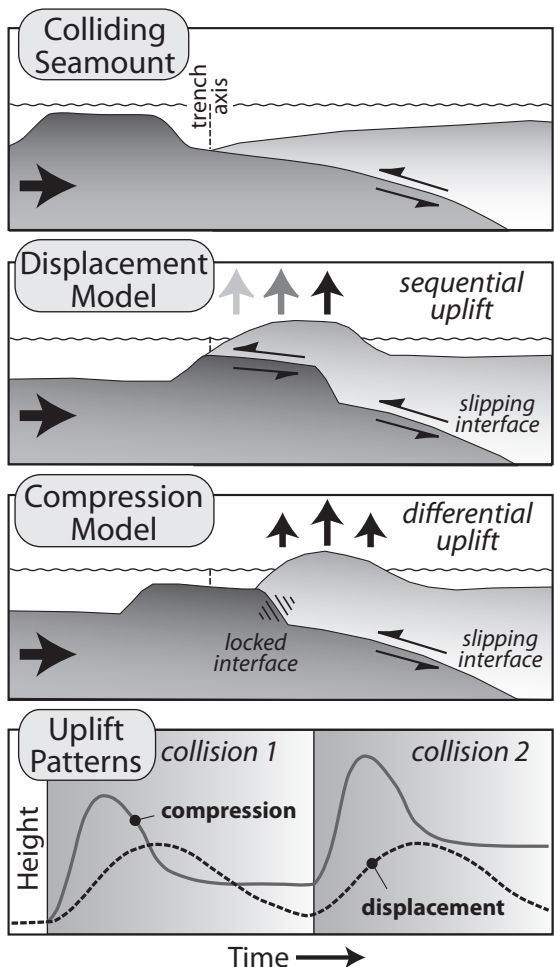


Fig. 9.3 Models of forearc deformation for a subducting seamount.

Colliding seamount (top), representing thickened crust, approaches the forearc, where its collision could cause distinctive patterns of deformation. In the “displacement model,” the seamount slides beneath the forearc, thereby driving accelerated uplift that migrates landward and gradually decelerates in its wake. In the “compression model,” the seamount gets stuck as it impinges on the trench and forearc. The locked interface translates the collisional stresses inland and initially causes abrupt and rapid uplift. If the locked interface then ruptures and dismembers the seamount, subsidence will also be rapid. Each model predicts a different temporal and spatial pattern of uplift (bottom). Modified after Taylor *et al.* (2005).

geomorphic markers. Second, some landscape responses are described, using examples of growing faults and folds, deforming forearcs, and tilted mountain ranges.

Calibrating rates of deformation

Marine terraces

Several approaches can be employed to define the vertical deformation pattern along a coastline using either abrasion platforms or coral terraces (Figs 2.1 and 2.2). A rising coastal landmass is like a strip chart that records and uplifts the geological record of each successive sea-level highstand. As in all rate studies, one needs knowledge of the initial and final elevation of a marker, as well as the time it took to traverse that vertical distance. The key here is that the landmass is assumed to be rising steadily (with good enough data, this assumption can be tested), whereas sea level is varying widely over glacial-interglacial cycles that have periods on the order of tens of thousands to one hundred thousand years. The abrasional or constructional platform that is created at time zero is a nearly planar, gently sloping surface. Subsequent emergence of a platform implies that the rock mass has moved upward relative to sea level, and submergence implies the opposite. In order to know which has moved, the sea or the land, other information (e.g., eustatic records) must be brought to bear. On the other hand, any warping of this surface can be used directly and unambiguously to document relative movement of one part of the coastal landmass with respect to another. Depending on what is already known about the landscape, one can either use the terraces to deduce a sea-level curve, or use the terraces to deduce the rate of uplift of the landmass. In any case, in order to document rates of deformation, one must be able to date the platforms.

The determination of the absolute ages for former sea levels has been something of an industry for a large number of researchers for several decades. Unfortunately, most of the sea-level highstands that we would like to date are older (>40 ka) than can be dated using ^{14}C

approaches. As described in Chapter 3, uranium-series (U-Th) dates on aragonitic material have provided ages of surfaces several hundred thousand years old. With improved techniques and measurement capabilities, uranium-series dates have become increasingly precise, such that dates of 100 ka may have measurement uncertainties of $<1\%$ (Edwards *et al.*, 1997), and chronologies of sea-level changes have been extended back to greater than 200 ka (Andersen *et al.*, 2010; Edwards *et al.*, 1997).

In the ideal case, we have a reliable global (eustatic) sea-level curve (sea level relative to present versus time; Fig. 2.5) and a flight of dated terraces. The age and the present elevation of each terrace (relative sea level) with respect to the position of the correlative eustatic sea level at the time of terrace formation can be used to define amounts and rates of rock uplift through time. But, what if the terraces are undated, or only one of them has an approximate age? Can they still be used to define the uplift rate? In this situation, one typically assumes a steady uplift rate (or assigns one, if a single terrace is dated), and then determines graphically (or numerically, on the computer) how well the observed heights of terraces correlate with the predicted position of terraces based on the eustatic sea-level curve and the constant apparent sea-level change (Fig. 9.4A).

In this graphical matching technique, a terrace should exist at an appropriate height above sea level for each of the high sea-level peaks defined in the eustatic curve. If the elevation of each sea-level highstand matches with that of a preserved terrace, then the assumption of constant uplift appears warranted. If the match is poor, then a different uplift rate can be tried. If the match is still unsatisfactory, the rate of uplift might be varied through time in order to obtain a satisfactory match (Fig. 9.4B). If one permits the uplift rate to vary without constraint, however, a perfect, but probably meaningless, match can always be obtained. The simplest and often most convincing approach, therefore, assumes a constant uplift rate. If rates are varied through time to obtain a match, then a geologically reasonable rationale for the proposed

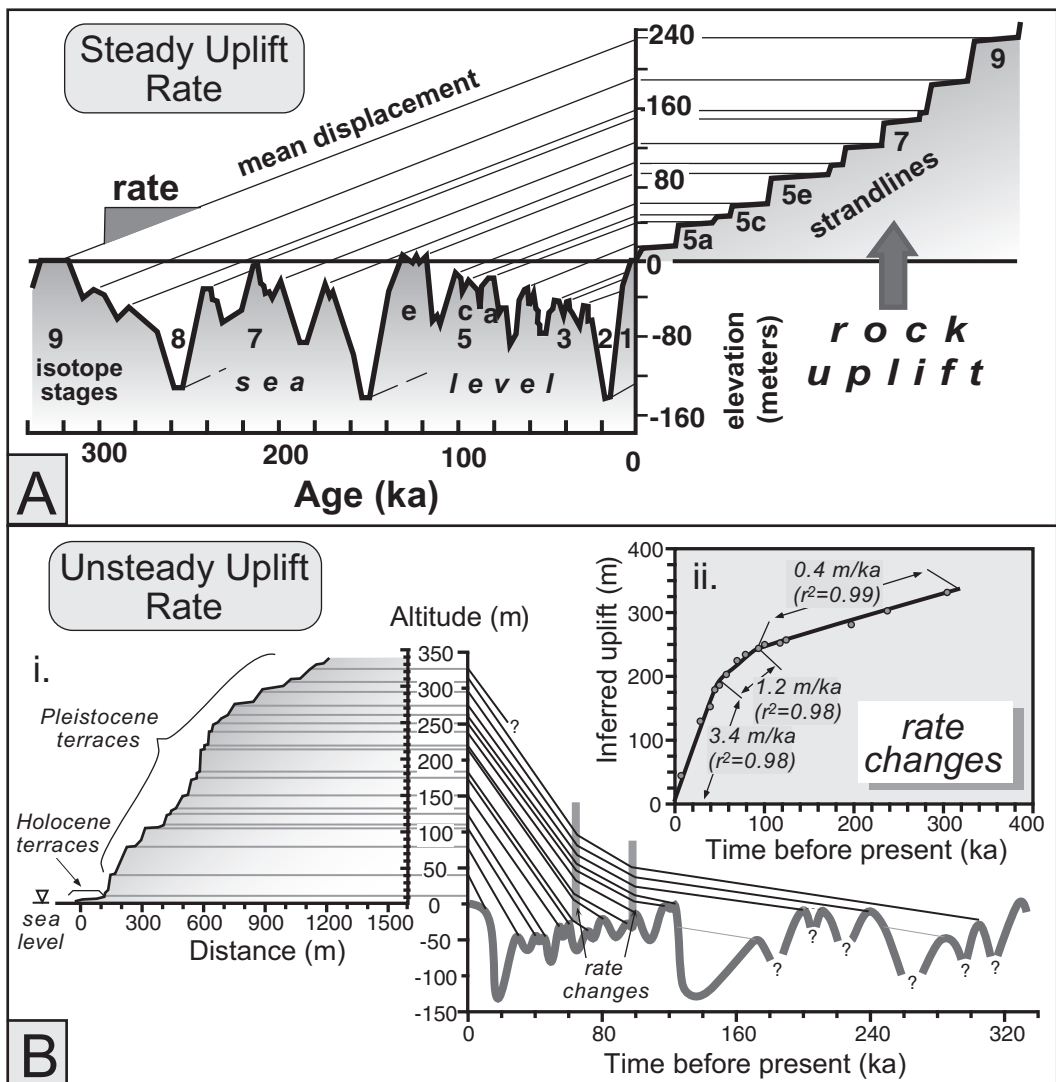


Fig. 9.4 Correlation of sea-level curve with uplifted marine terraces.

A. Graphical correlation of sea-level variations with coastal terrace record based on a steady rock-uplift rate. Note that not all highstands older than 130 ka or younger than 50 ka are represented in the terrace record. Some older ones are obscured by subsequent higher sea levels, whereas some younger ones are still below sea level. Modified after Lajoie (1986). B. i. Example of terrace correlation in northern California based on the assumption of abrupt accelerations in the rate of uplift. This coastal area has been strongly affected by the passage of the Mendocino triple junction during the past 100 kyr, such that accelerated uplift is not unreasonable. ii. In order to correlate each of the observed terraces with a sea-level highstand, the Middle Pleistocene rate of bedrock uplift is inferred to have tripled at ~100 ka and then to have tripled again at ~60 ka. Modified after Merritts and Bull (1989).

changes should be offered for this variation. One observation that could support an assumed acceleration in the rate of uplift would be the presence of older, higher terraces that are more

closely vertically spaced than younger, lower terraces (Fig. 9.4B). Given the nature of the sea-level curve in which the frequency of high sea-level stands appears lower prior to 125 ka,

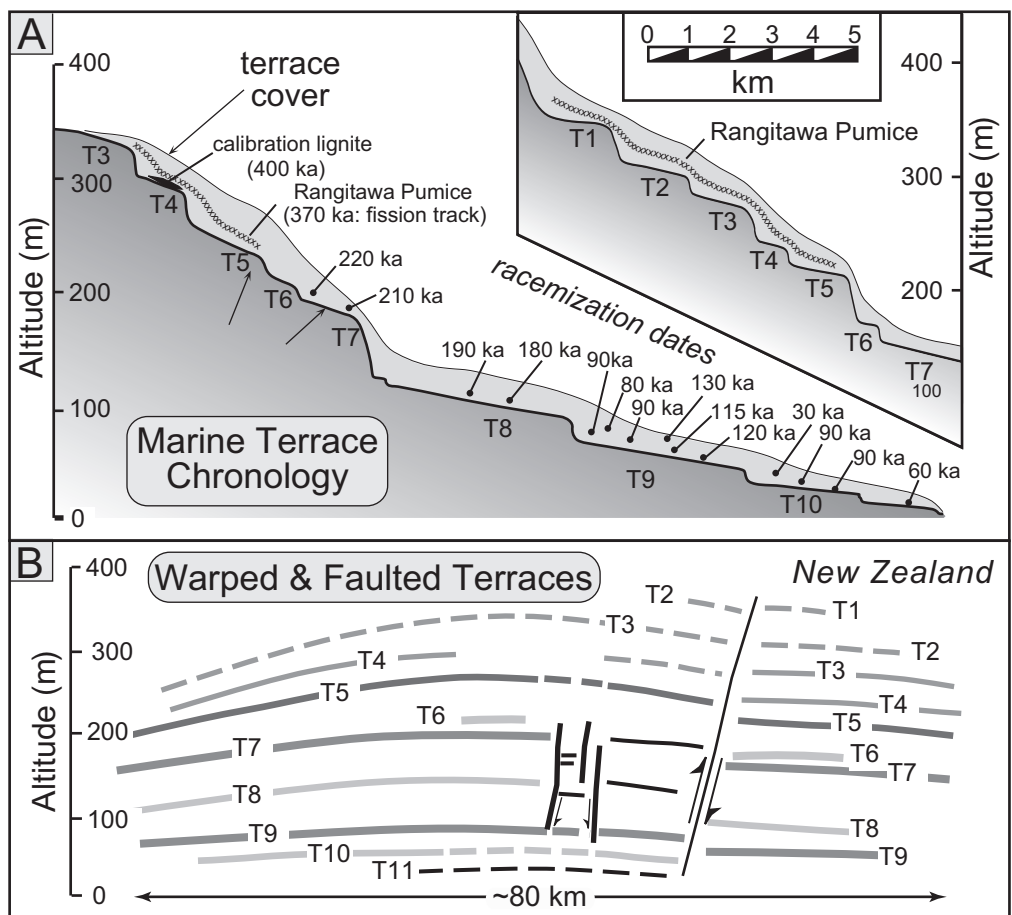


Fig. 9.5 Dated and deformed marine terrace sequences in New Zealand.

A. Terrace chronology developed using fission-track dating on pumice and amino acid racemization dating on organic material overlying the terraces. These dates span more than 300 kyr and provide minimum ages for each terrace. Correlation among sections is based on pumice, soil stratigraphy, and geomorphic position. B. Same terraces warped and offset across faults along 80 km of coast. Tracing and correct identification of terraces is key to discovering any offset across faults. The progressively greater offsets of older terraces indicate that the fault has been periodically active throughout the period of uplift. Note the difference from a faulted trench stratigraphy (Fig. 6.3) in which the strata at lower elevations record more displacement than those higher in the trench walls. Modified after Pillans (1983).

such a spatial distribution of terraces argues for an increase in uplift rates. Be aware, however, that the younger sea-level record is better known and that its complex and rapid changes have emerged from recent success with high-precision dating. Similar sea-level complexity (and multiple, closely spaced highstands) may also be documented in the pre-125-ka record when we develop a similar chronological precision.

If flights of marine terraces can be correlated with the sea-level curve at numerous sites along

a coastline, or even if they can only be laterally correlated from one site to the next, these data can be used to define patterns of differential vertical uplift. Abrupt offsets in terrace heights with increasingly larger separations for successively older terraces on the one side will indicate the presence of persistently active faults (Fig. 9.5A and B), whereas steady convergence or divergence between individual terraces of a given age will exemplify broad warping of an area.

The deformed patterns of uplifted Pleistocene terraces are an obvious and readily observed consequence of variable bedrock uplift rates in coastal regions. Moreover, comparisons of the shapes of deformed terraces of different ages allow one to assess spatial and temporal variability in rock uplift rates. Commonly, the faults that are responsible for uplift of the terraces are either blind faults or break the Earth's surface below sea level. In such circumstances, these warped terraces take on added significance, because they may permit testing of hypotheses about the behavior of unexposed faults or folds that are thought to be responsible for their uplift. For example, comparisons of coseismic coastal uplift patterns with patterns of warped terraces can be used to assess whether a long succession of characteristic earthquakes on one or two local faults could have generated the observed terrace pattern. Such a situation was previously described (see Fig. 4.8) on the California coast in the vicinity of Santa Cruz, where uplifted and broadly warped marine terraces are well preserved. Alternatively, the geometry of warped terraces on the flanks of a growing anticline can be used to deduce the orientation and typical slip direction along the buried fault(s) responsible for terrace uplift (Ward and Valensise, 1994). The terraces are like bathtub rings around a growing fold: each one originally formed a horizontal surface (see Box 9.1). But now, in their deformed positions, their geometry can be inverted to estimate the depth, dip, and slip on underlying faults.

Most marine abrasion platforms vary from 100 to 500 m wide. The depth to wave base and the requirement that the seaward slope of the platform permits removal of debris from the shoreface appears to control the maximum platform width. In some areas, however, platforms greater than or equal to 1 km wide are preserved (e.g., Fig. 9.5A). Unusually wide terraces are likely to result from one of two conditions: the presence of very weak, readily eroded rocks; or successive reoccupations of a given terrace level. If the amount of bedrock uplift between two highstands is just a bit less in magnitude than, but in the same direction as,

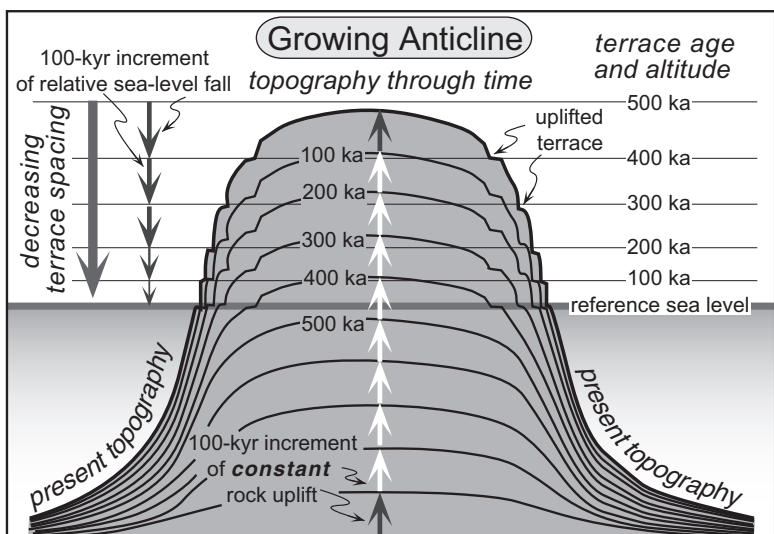
the vertical difference in sea level between the two highstands, then a previously formed terrace can be reoccupied by a slightly higher sea level and laterally extended (Kelsey and Bockheim, 1994).

It is important here to note that there exists a "terrace survival problem" analogous to the glacial moraine survival problem (see Box 2.3). A sequence of elevations corresponding to a terrace flight at one location along a coastline might be different from another nearby sequence in that one or more terraces might be missing (Anderson *et al.*, 1999). This mismatch results from the fact that: (i) platform width is dependent on very local variables such as lithology, structure, and orientation of the coastline relative to the dominant wave energy (Adams *et al.*, 2005); and (ii) a younger terrace platform grows in width at the expense of older platforms, whose outer edges are progressively nibbled away by the cliff at the back of the younger terrace. Hence, younger terraces can locally eliminate older ones. In addition, this geomorphic reality raises a cautionary flag against using platform width as a correlation tool.

Until recently, only emergent platforms were used in defining uplift patterns. This limitation has changed with the advent of increasingly available and detailed bathymetry and with new drilling methods that allow collection of geological materials from the sea floor or from beneath younger sediments. An example of the use of sub-sea-level platforms utilizes corals dredged from about 2 km deep on a submerged platform in the Huon Gulf of the Solomon Sea (Galewsky *et al.*, 1996). These ancient platforms were first visualized using sidescan sonar and detailed bathymetry, where both anomalously flat surfaces and striking spires (interpreted to be coral pinnacles) were identified as potential targets for dredging. Samples retrieved from these surfaces were dated at approximately 340 ka using uranium-series dating and, thereby, revealed a long-term subsidence rate of about 6 mm/yr, one of the first documentations of such sustained rates. With the explosion of high-resolution sea-floor data, the use of submerged terrace platforms promises to become more routine.

Box 9.1 Marine terraces on a growing fold.

In addition to the effects of differential warping or fault offsets on terrace patterns, one can wonder how a changing sea level would interact with a three-dimensional deforming shape, such as a growing fold that is increasing in amplitude through time. Some simple models of a growing anticline (Ward and Valensise, 1994) predict patterns of strand lines that are not intuitively obvious. In the model (see figure), a fold grows above a buried thrust fault in such a manner that the crest of the fold is uplifted at a steady rate through time. Every 100 kyr a new terrace is cut into the margins of the fold during a highstand, referred to here as a reference sea level. Thus, one might expect that, given a uniformly growing fold and terrace-cutting episodes regularly spaced in time, the terraces would show a uniform spatial distribution. Such spacing is not borne out in the model, however, because the emergent part of the fold becomes broader through time.



Model of marine terraces etched into the flanks of a growing anticline. Modified after Ward and Valensise (1994).

Although uplift is steady at any point along the fold, it decreases from the crest of the fold toward its flanks. Therefore, younger terraces that are formed on the ever-widening fold as it emerges above sea level are spaced more closely than older terraces formed when the emergent fold was narrower. Whereas the changing vertical spacing of the terraces, such as those depicted here, would often be interpreted as indicating a steady deceleration in the rate of uplift, the variable spacing is in fact a simple consequence of the shape of the steadily growing fold. This model would predict a uniform vertical spacing of terraces only in situations where the coastal region is experiencing a block-like uplift. Thus, in analyzing any coastal terrace sequence, the cause of the oceanward slope of the land surface should be considered. Is it a result of folding such that interior regions have been uplifted more rapidly than the coastal area? Or is it a geomorphic surface created in the absence of differential tilting? Given the model predictions described here, the distinction between a tectonically created slope and a geomorphic slope is fundamental to making a reliable interpretation of a terrace succession.

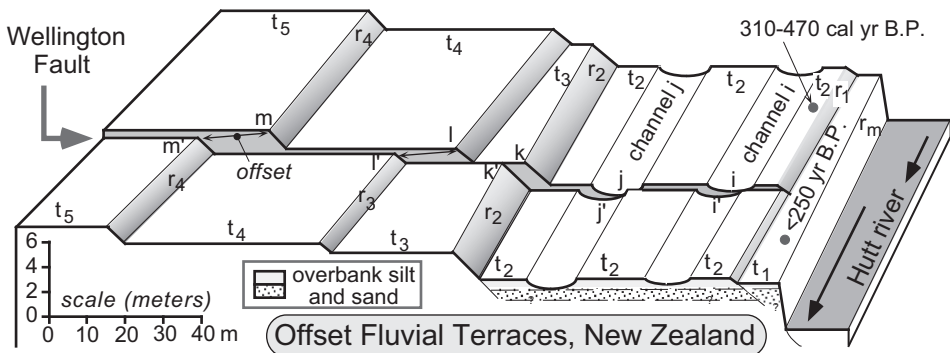


Fig. 9.6 Displaced fluvial terraces along the Wellington Fault, New Zealand.

The lowest terrace, dated at <250 yr, is not displaced by this strike-slip fault, whereas the next highest terrace (t_2) and the channels cut across its surface show a displacement of ~4 m attributable to the last major earthquake. Note that any fault displacement of the riser (r_1) between t_2 and t_1 was beveled off during creation of t_1 . The amount of offset of the risers increases systematically with each older terrace. Important controls on terrace width are exerted by the geometry of the river channel prior to abandonment (note the triangular shape of t_3). The vertical throw across the fault is small (~10%) compared to the horizontal displacement. Modified after Van Dissen *et al.* (1992).

Fluvial terraces

When a river course flanked by flights of fluvial terraces is oriented at a high angle to a strike-slip or dip-slip fault, the terraces displaced by the fault can provide an excellent record of progressive offsets. If some or all of the terraces can also be dated, then the rates of fault displacement over the duration of the dated sequence can be derived. In regions where climatically controlled terraces are widespread, it may not be necessary to date the terraces directly adjacent to the fault, because sequences of soils, loess, or volcanic ashes that overlie the terrace treads may permit correlation with other, better dated, terraces in the same region.

The assessment of offset fluvial terraces requires several steps. First, the correlation of terrace treads and risers across the fault must be determined. Because of changes in the river course through time, the height of risers between terraces along strike-slip faults is generally a better guide to correlation than is the width of the terrace tread, which is sensitive to patterns of lateral migration by the former channel. If, however, significant vertical (dip-slip) displacement has occurred along the fault, then riser height will vary as well. In any case, the

most reliable correlation will usually result from consideration of the entire suite of treads and risers and any relative or absolute dating of their surfaces. Second, the offset of formerly continuous risers is measured across the fault for each terrace level. In addition, any other linear features, such as channels or gullies, located on the terrace treads and trending across the fault are also measured (Fig. 9.6). As described earlier (Box 6.1), careful attention should be paid to whether risers have been modified since the upper tread was abandoned and whether slip rates should be based on ages for the upper or lower treads that bracket the riser. Finally, to the extent permitted by available dates, a history of cumulative offset and rates of offset through time is developed.

Although a similar methodology could be applied to marine terraces that have been cut by strike-slip or dip-slip faults, fluvial terraces have a considerable advantage in terms of reconstructing the record of the past 10–50 kyr because the available terrestrial record in this interval is commonly more complete. Whereas climatically driven changes in water and sediment discharge between 10 and 50 ka have generated multiple fluvial terraces in many sites, sea level was below present for this entire

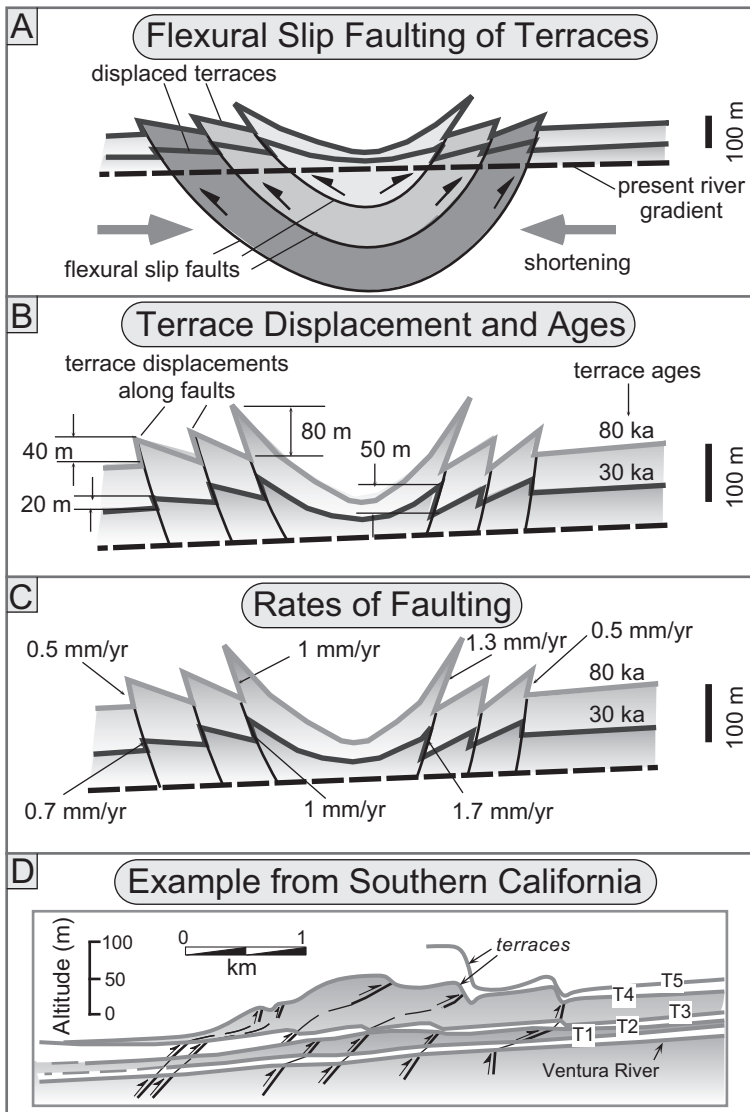


Fig. 9.7 Terraces displaced across flexural slip faults.

A. Geometry of terrace displacement defines greatest displacement near the core of the fold. B. Terrace ages and displacements of terraces across different faults. Note that offsets are not symmetrical across the synclinal axis and that younger terraces display lesser offsets compared to the older terraces. C. Rates of fault displacement based on offset of dated terraces. Note that rates are not necessarily constant along the same fault through time. D. Displacement of terraces by flexural slip faults along the Ventura River, California. Ages assigned to the terraces are 92 ka (T5), 54 ka (T4), 38 ka (T3), 30 ka (T2), and 17 ka (T1). Modified after Rockwell *et al.* (1984).

interval (Fig. 2.5), such that, with the exception of rapidly rising coasts, marine terraces younger than 80 ka are still commonly submerged.

Where rivers cross active folds or dip-slip faults, fluvial terraces can also record progressive displacement. Where faults rupture the surface, it is expected that the age and height of the terrace will generally correlate with the magnitude of cumulative displacement (Plate 5). Flights of fluvial terraces can overcome some of the limitations imposed on paleoseismological

studies by the fact that trench walls in alluvium are often unstable, so that deeply excavated trenches are uncommon. Trenches in any of the terrace risers may reveal paleoseismological data on the last few ruptures that display perhaps a few meters of displacement in each rupture. In contrast, the entire vertical suite of terraces can serve to define the long-term displacement history, such that several tens to hundreds of meters of displacement can be recorded by the higher terraces (Plate 5). As

with any study seeking to define rates, key constraints are provided by dating of the formation and abandonment of each terrace.

Across actively deforming zones in which multiple faults are closely spaced, a single terrace may be displaced by several faults. Even without knowledge of the terrace age, the variable displacement of the marker surface by each fault will indicate how deformation has been partitioned among the active structures, and relative rates of displacement can be defined. Because flexural slip faults (Plate 6) exploit weak interbeds as slip surfaces, the limbs of tightening synclines sometimes display fairly closely spaced faults (Figs 4.34 and 9.7). Studies along the Ventura River in southern California of terraces offset across flexural slip faults in the Canada Larga syncline (Rockwell *et al.*, 1984) provide well-calibrated examples of both progressive terrace displacement and differential partitioning of displacement among several faults (Fig. 9.7D).

In the case of growing folds, warped fluvial terraces can provide unique insights into the two-dimensional geometry of the fold and its rate of growth. Antecedent streams that maintain their courses across growing folds will often produce strath terraces that may or may not be mantled with a veneer of alluvial debris. The terraces develop during intervals when lateral abrasion dominates over vertical incision (Figs 2.12 and 7.13). In cases in which (i) terraces have extensive, down-valley continuity and (ii) the deformed treads within a rising structure, such as a fold, appear to grade into undeformed treads beyond the structure, it is likely that climatic fluctuations controlled the periods of major terrace formation. Alternatively, if the growth of the structure itself was tectonically pulsed, then terraces may have formed during intervals of reduced deformation rates (e.g., Lu *et al.*, 2010). Most published work (Medwedeff, 1992; Suppe *et al.*, 1992; Vergés *et al.*, 1996; Hubert-Ferrari *et al.*, 2007) in which rates of fold growth are well calibrated, however, is inconsistent with a pulsed deformation model.

It is worth stressing that a crucial component in the analysis of both marine and fluvial terraces is the correlations that are drawn between physically isolated terrace remnants.

Often, erosion makes it impossible to trace terrace surfaces confidently, even along smoothly folded structures. Whenever faults are encountered, correlation of terraces across the fault becomes even more difficult. Because interpretations of offsets are entirely dependent on such correlations (Fig. 2.17), characterization of the terrace surface and its subsurface stratigraphy is often a major element in any such study (Merritts *et al.*, 1994). Soil development, loess stratigraphy, tephra layers, and relative and absolute dating techniques can all be used to distinguish between and correlate among terraces.

Landscape responses at intermediate time scales

We distinguish here between landscape features that permit a direct calibration of deformation rates, such as terraces, and features that represent part of the landscape response to deformation. Calibration features primarily comprise displaced geomorphic markers whose initial shape is quite well known. The initial geometries of most other elements in the landscape, ranging from stream channels to hillslopes, are less easily traced backward in time, because these geometries represent an integrated response to ongoing deformation, base-level variation, and climate change. These features, therefore, only indirectly calibrate rates of deformation.

Stream gradients

River networks represent a hierarchical organization of tributary streams (lower order) routing flow into trunk streams (higher order). For a graded river flowing across uniform rock types and experiencing uniform uplift, the downstream channel gradient gets systematically gentler as a function of increasing discharge, which itself tends to vary as a function of catchment area (Fig. 8.5). Departures of the river gradient from this idealized, smooth shape may reflect variations in the rock strength of the river bed or variations in rock-uplift rate. Numerical models of tectonically perturbed rivers predict

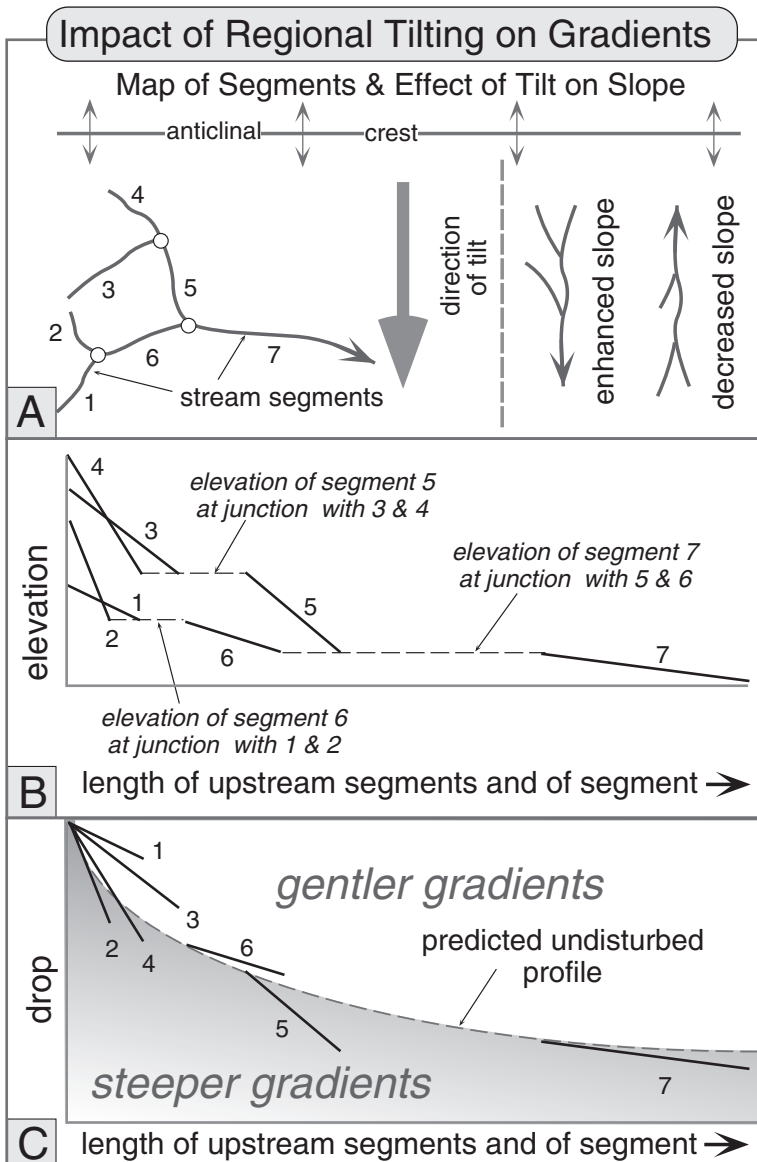


Fig. 9.8 Gradient analysis of tilted stream segments.

A. Stream network is divided into segments based on positions of stream junctions. The model assumes that, if tilting is occurring, streams flowing in the direction of tilting will have increased gradients, whereas those flowing in the opposite direction will have gentler gradients. B. Depiction of stream gradients. Each stream segment is plotted according to its length and to the elevation of the upper and lower ends of the segment. The upstream end of the segment (on the x axis) is determined by the length of segments that are upstream of it and tributary to it. Thus, segments 1 and 2 flow into segment 6, segments 3 and 4 flow into segment 5, and segments 5 and 6 flow into segment 7. Segments 1 to 4 all represent first-order tributaries that have no upstream segments – their upper ends plot on the left-hand margin. The sum of the lengths of segments 1 and 2 determines the horizontal position of the upstream end of segment 6 into which they flow. C. Departure from ideal gradient. When compared to the idealized gradient, steeper segments suggest tilting in the downstream direction. Compare the relative sense of tilting with the hypothesized fold orientation in the top panel. Modified after Merritts and Hesterberg (1994).

that they will approach a graded profile rather rapidly (Snow and Slingerland, 1987) once the perturbation ceases. Thus, anomalously steep or gentle river profiles, especially when not correlated to lithologic contrasts, may be interpreted as responses to ongoing tectonism.

Several approaches use data extracted from topographic maps to identify areas of active deformation, such as zones where stream gradients depart from expected longitudinal

profiles. Consider a region experiencing tilting toward the south. Rivers flowing south will tend to have their gradients steepened, whereas rivers flowing north will have their gradient lessened with respect to untilted regions. One approach to the analysis of tilted channel networks (Merritts and Hesterberg, 1994) begins by segmenting a drainage network into its component tributaries (Fig. 9.8A) and measuring (i) the length of each segment and

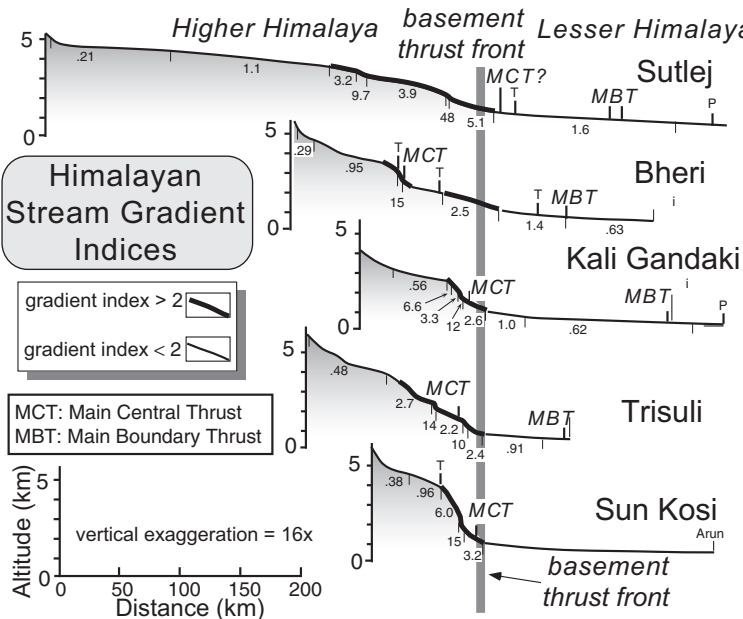


Fig. 9.9 Longitudinal profiles and stream-gradient indices for Himalayan rivers.

Thicker segments of the profile indicate reaches where the local gradient index (SL) is more than twice the index (k) for the entire profile: $SL/k \geq 2$. The steepest gradients are not associated with the Main Boundary Thrust or active deformation to the south. Rather, they occur near the Main Central Thrust and appear to result from upward ramping of the overthrusting Himalaya above a deep-seated basement thrust. Modified after Seeber and Gornitz (1983).

(ii) the elevation of its upper and lower ends. The elevation range of each segment (y axis) can then be plotted against the sum of the lengths of the upstream segments and the length of the segment itself (x axis) (Fig. 9.8B). The lower elevation of each feeder or tributary segment is matched to the upper elevation of each segment into which it flows. Subsequently, using the x axis position as dictated by the length of the upstream segments, each segment is compared with an idealized logarithmic longitudinal profile (Fig. 9.8C). Significant departures from the ideal profile serve to identify segments that could be interpreted to indicate increased or decreased gradients over time due to tilting. When coherent areas are located in which all or most of the streams flowing in a given direction show the same tendency toward steepening or flattening, regional patterns of warping can be deduced (Merritts and Hesterberg, 1994). One must, however, exercise considerable caution in the application of such a technique, as it rests on the assumption of an “ideal” profile, and all effects of the variations in lithology or grain size of the material involved in the fluvial system must be assumed to be small compared to the tectonically induced changes in slope.

Before digital topographic data became widely available, departures from expected channel gradients were sometimes identified on the basis of changes in the stream-gradient index (SL), which compares the slope of a local reach with the distance to the drainage divide (Hack, 1973). For a short reach, the stream-gradient index can usually be approximated by

$$SL = (\Delta H / \Delta L)L \quad (9.1)$$

where L is the distance measured from the drainage divide to the mid-point of the reach, and the slope of the short reach ($\Delta H / \Delta L$) is considered constant. For a well-adjusted channel profile, the stream-gradient index will remain nearly constant or change only slowly. Abrupt increases in the index typify oversteepened reaches.

A pioneering study of major Himalayan rivers by Seeber and Gornitz (1983) used stream-gradient indices to identify those river reaches that were anomalously steep (Fig. 9.9). Their analysis clearly showed that the steep reaches were not associated with what were considered the younger, active faults, such as the Main Boundary Thrust (MBT; Fig. 9.9), but instead were localized either above a deeply buried thrust ramp in the basement or near the trace

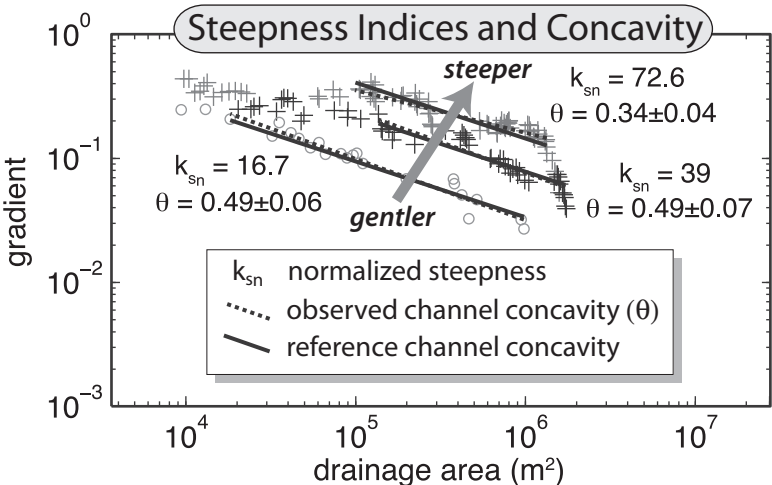


Fig. 9.10 River channel steepness indices and concavity.

Forced regressions through slope-area data using a reference concavity (0.45 in this example) define differences in normalized channel steepness (k_{sn}). For these channels, the observed concavity (θ) is similar to the reference concavity, but normalized steepness varies five-fold. Note the difference in channel slope between the channels for any given drainage area. Modified after Kirby *et al.* (2007).

of the Main Central Thrust (MCT; Fig. 9.9). This study helped promote a new view of this collisional orogen in which rates of rock uplift, large-scale crustal structure, and regional topography became inextricably linked.

With the widespread availability of digital topography and of programs based on geographic information systems (GIS) that are designed to analyze such topography, the use of stream-gradient indices has been largely replaced by use of a steepness index, k_s (Wobus *et al.*, 2006a). Recall from the previous chapter that $S = k_s A^{-\theta}$ (Eqn 8.7), where S is slope, k_s is the steepness index, A is upstream catchment area, and θ is concavity (see Fig. 8.4). Although concavity varies among rivers, it typically ranges between 0.4 and 0.7 (Whipple, 2004). For the sake of comparison among different rivers, the steepness index can be normalized, k_{sn} , by using the same reference concavity, θ_{ref} , for all channels being analyzed, such that

$$k_{sn} = k_s A_{cent}^{-(\theta_{ref} - \theta)} \quad (9.2)$$

where A_{cent} is the area upstream of the mid-point of the reach being analyzed in the DEM (Wobus *et al.*, 2006a). In practice, this approach finds

the normalized steepness, k_{sn} , when a regression with a fixed reference concavity (commonly 0.45) is forced through channel slope versus area data to yield the best fit (Fig. 9.10). Combined Matlab and GIS programs that analyze a DEM and make a spatial map of variations in normalized steepness can currently be downloaded from <http://www.geomorphotools.org>. Such maps can permit ready identification of river reaches or whole regions characterized by anomalous steepness.

Analyses of river profiles on a rapidly deforming fold (Kirby and Whipple, 2001) have shown that high concavities characterize rivers whose headwaters are uplifting more rapidly than more downstream reaches (Fig. 8.24), but that concavities are commonly normal for a channel exposed to a uniform uplift rate, irrespective of whether it is rapid or slow. We might then wonder what happens to concavity and steepness when the rate of uplift changes at a given site. From a theoretical perspective, we can predict that, if the relative uplift rate doubles (for example, by accelerated fault slip at the channel's outlet), a knickpoint will develop that propagates upstream and that, downstream of the knickpoint, the channel will become steeper in order to erode at a rate that balances the new uplift rate (Fig. 9.11).

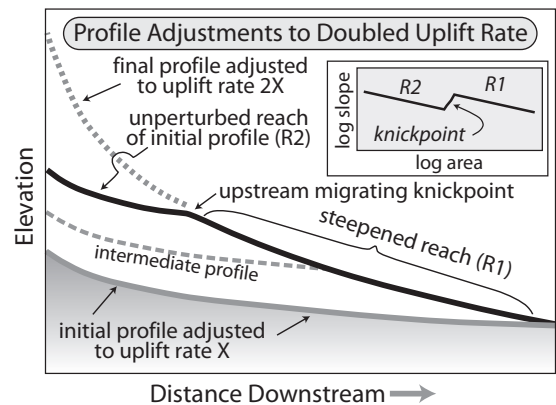


Fig. 9.11 River-channel adjustments to accelerated uplift.

Channel profile in a transient state due to doubling of the uplift rate with respect to the outlet. As a knickpoint sweeps upstream, the lower channel profile (R1) steepens, whereas the upper profile (R2) retains its initial gradient, one that was adjusted to the original uplift rate. Once the knickpoint sweeps to the headwaters, the entire profile will be steepened. Inset shows lower and upper reaches in slope-area space. Note the different steepnesses (vertical position of the line with respect to area), but same concavities (slope of the line). Modified after Whipple and Tucker (1999).

Upstream of the knickpoint, the pre-acceleration gradient will persist, because that part of the channel will not “feel” the acceleration at the outlet until its effects are translated upstream by the knickpoint (Whipple and Tucker, 1999).

One well-documented region where both spatial and temporal changes in rock uplift rate have occurred is the northern Californian coastal region. Here, over the past few million years, the Mendocino triple junction has swept northward across the region and created a wave of accelerated uplift followed by gradual restoration of rates in the wake of the triple junction (Merritts and Bull, 1989). Studies of coastal terraces, such as that depicted in Fig. 9.4, reveal more than six-fold increases in uplift rates over the past 100 kyr for some sites, thereby providing a striking context in which to examine channel responses to these differences in rates. Whereas the southern part of the region has sustained uplift rates $<0.5 \text{ mm/yr}$ for the past 300 ka, the northern region accelerated to $3\text{--}4 \text{ mm/yr}$ at $\sim 100 \text{ ka}$. Despite these strong contrasts in uplift rates, channel concavity, θ , remains nearly constant (Fig. 9.12) throughout the study area (Snyder *et al.*, 2000). Such constancy suggests that (i) the channels are in rough equilibrium with

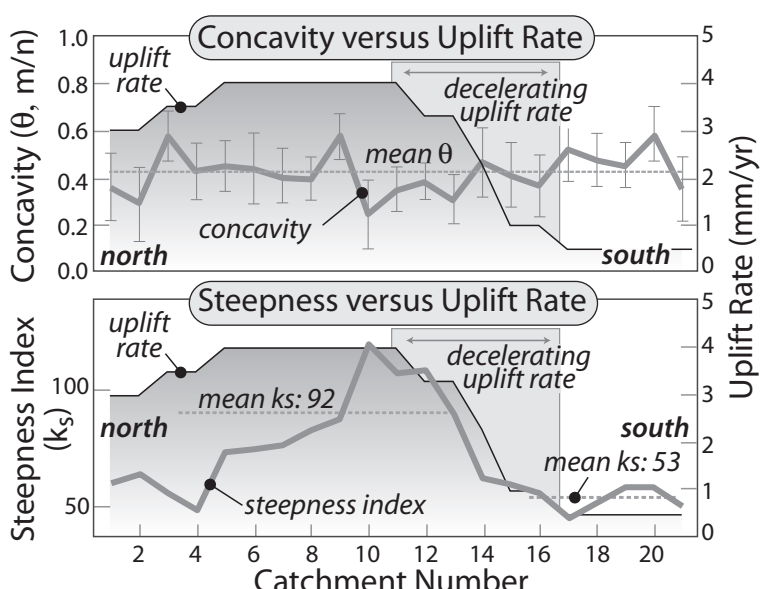


Fig. 9.12 Channel concavity and steepness in different uplift regimes.

Rates of rock uplift deduced from marine terraces define rates range from $<0.5 \text{ mm/yr}$ to 4 mm/yr along the northern California coast (Merritts and Bull, 1989). (Top)

Concavity is largely insensitive to uplift-rate variations. Mean concavity is ~ 0.45 , consistent with expectations for adjusted channels. (Bottom) Steepness shows strong contrasts, with higher average steepness in the high-uplift-rate zone. Note correlation of steepness index with uplift rate across the zone of decelerating rates. Modified from Snyder *et al.* (2000).

the uplift rate and (ii) channel-profile adjustments to the increased rates have occurred in less than 100 kyr, the time when rates accelerated. In contrast to the constant concavity, channel steepness shows strong regional variability (Fig. 9.12). The steepness index, k_s , is nearly twice as large in the high-uplift-rate region as in the low-rate region. Notably, the uplift rate and steepness index co-vary in the zone of changing uplift rates (catchments 12 to 16; Fig. 9.12). In the northernmost catchments, however, the steepness index decreases despite the rather high uplift rate. Although the cause for this decoupling is not known, orographic rainfall is about twice as great in the north than in the south (Snyder *et al.*, 2000). To the extent that the efficiency of erosion is linked to the mean annual discharge, higher rainfall could drive more erosion and promote less steep channels for a given erosion or uplift rate.

From landscapes to faults

Sometimes one of the biggest challenges for field geologists is simply recognizing the existence of major faults. Such faults may be blind, they may rupture the surface where few geomorphic markers exist with which to recognize differential displacement, or dense vegetation may obscure clear views of offset features (e.g., Fig. 1.5). The identification of faults under these conditions commonly requires a quantification of landscape attributes that respond to the uplift or subsidence caused by active faults.

A recent study of the region surrounding Mount Tamalpais along the northern San Andreas Fault (Kirby *et al.*, 2007) exploits changes in mean topography, channel steepness indices, hillslope angles, and topographic relief to delineate a spatial gradient that is interpreted as a response to a blind thrust (Fig. 9.13). Along a transect southwards toward Mount Tamalpais, both the mean and maximum elevations rise, as does the average steepness of hillslopes and the fraction of slopes considered to be at a threshold angle for failure. Steepness indices for a suite of similarly sized catchments along this north-south transect show an exponential

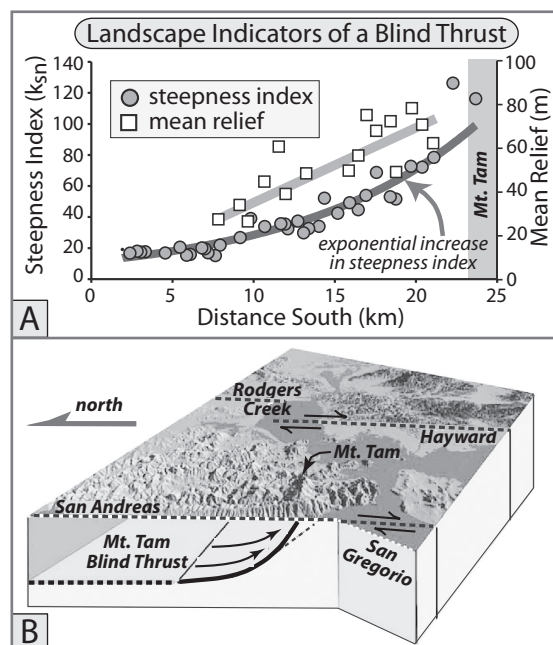


Fig. 9.13 Topographic indices related to differential uplift above a blind thrust.

- A. Normalized steepness index (reference concavity = 0.45) and relief in the inner gorge as a function of distance. Both parameters increase towards the south to where Mount Tamalpais is located (~24 km) and suggest a concomitant increase in rock uplift rates.
- B. Schematic model for an uplift gradient above a listric blind thrust. Vertically exaggerated topography and major dextral strike-slip faults are shown. Modified after Kirby *et al.* (2007).

increase toward the south (Fig. 9.13A). Channels in all these catchments display inner gorges whose walls are at threshold angles, suggesting that these walls are eroding by bedrock landsliding, presumably because the channels are incising at rates faster than soil-mantled hillslopes can erode. The relief from the channel bottom to the top of the inner gorges also progressively increases toward the south (Fig. 9.13A) and is interpreted to indicate increasingly rapid rates of channel incision. The presence of an inner gorges, rather than a gradually steepening hillslope rising above each channel, suggests that this landscape is in a transient state. This suite of observations suggests that rock uplift rates increase

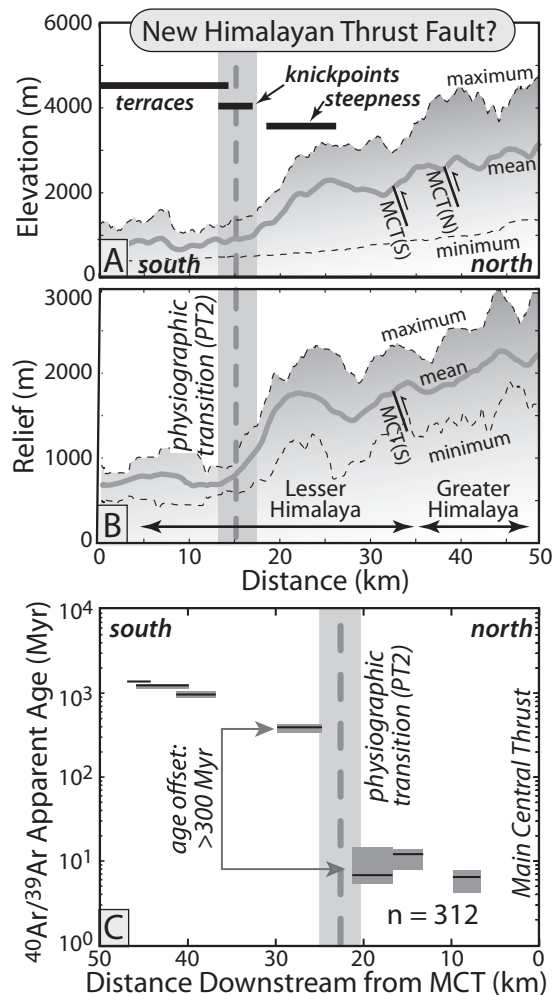


Fig. 9.14 Topographic indices and detrital ages related to a proposed Himalayan fault.

- A. Maximum, mean, and minimum elevation along a north-south swath focused on the Burhi Gandaki river in central Nepal (see Plate 7). The northern and southern traces of the Main Central Thrust (MCT) and the north-south extent of fluvial terraces, river knickpoints, and normalized channel steepness indices greater than 450 are shown. Major topographic changes occur >20 km south of the MCT at the “physiographic transition 2” (PT2). Note the upward deflection of the mean elevation toward the maximum, indicating a transient state north of the PT2.
- B. Maximum, mean, and minimum of local relief show an abrupt increase at the PT2. Transition between Greater and Lesser Himalaya is taken as the MCT(S).
- C. Detrital muscovite cooling ages ($n=312$) from seven tributary catchments indicating a >10-fold offset of ages across the PT2. Box widths correspond

systematically toward the south and toward Mount Tamalpais, a scenario consistent with slip above a blind listric thrust fault (Fig. 9.13B).

During efforts to locate previously unknown active structures, both regional maps and swath profiles of topographic characteristics can be very useful, particularly for identifying anomalies or trends. In a swath profile, spatial data on transects perpendicular to the long axis of the swath are assessed at successive steps (typically equivalent to the pixel size of the data) along the swath. The data from each transect can be examined statistically to define their attributes: commonly maximum, mean, and minimum of some characteristic. For a typical swath profile of elevation in most landscapes, the mean elevation will lie closer to the minimum than to the maximum. If the mean elevation approaches the maximum, this upward deflection of the mean is likely to indicate a transient state of adjustment to an accelerated uplift rate in which rates of hillslope lowering are not keeping pace with the rate of rock uplift (Fig. 9.14). Similarly, changes in the average hillslope angle or topographic relief can be a signal that the landscape has adjusted (or is adjusting) to changes in patterns or rates of rock uplift.

Recent studies in the Nepalese Himalaya have combined diverse topographic attributes with bedrock cooling ages to identify what may prove to be a major, active, and previously unrecognized fault (Wobus *et al.*, 2003, 2006b). The location of this fault was initially deduced from maps of hillslope angles and channel steepness indices that show an abrupt discontinuity that lies south of the Main Central Thrust and within the Lesser Himalaya (Plate 7). Swath profiles across this region show concurrent increases in both mean elevation and mean relief (Fig. 9.14A and B) and led to the naming of this topographic break as the “physiographic transition 2” (or PT2). (The PT1 lies at the break between the Tibetan Plateau and the Greater Himalaya.)

to the widths of sampled catchments orthogonal to the swath. Box top and bottom show the 25th and 75th percentiles, with horizontal lines indicating the median age. Modified after Wobus *et al.* (2003, 2006b).

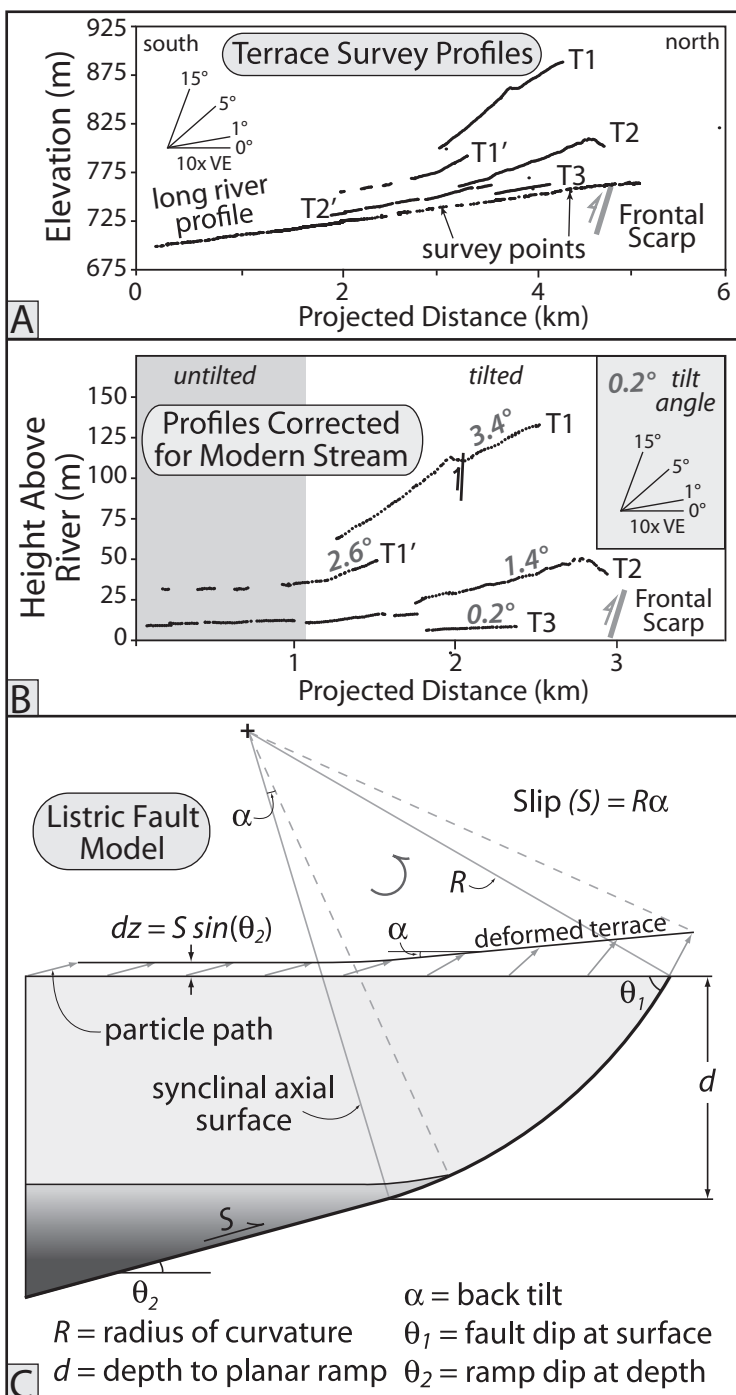


Fig. 9.15 Tilted backlimb terraces and listric thrust faulting.

A. Surveyed terrace and river profiles deformed above the Irishman Creek Fault, Mackenzie Basin, New Zealand. Terraces T1 to T3 span ages ranging from about 140 to 20 ka. B. Heights of terrace treads with respect to the modern river gradient. Note the progressively greater magnitude of tilting for older (higher) terraces, but the consistent position of the hinge representing the transition to the untilted domain (~1.2 km). C. Model for a listric fault linking to a planar ramp. When applied to the Irishman Creek data in panels A and B, the model predicts 190 m of slip on the T1 terrace, the listric-to-planar fault transition at 1.4 km depth, and a planar ramp dip of 17°. Modified after Amos *et al.* (2007).

Other changes observed at the PT2 include the abrupt northern end of Lesser Himalaya river terraces, commonly observed knickpoints in river profiles, and greatly increased channel

steepness to the immediate north (Fig. 9.14A). The totality of these topographic changes points to a higher rock uplift rate to the north of the PT2, but left open the question of whether this

rate change was due to a surface rupturing fault or a change in the ramp angle of a deeply buried fault surface. Wobus *et al.* (2003, 2005) also showed that a major discontinuity in the $^{40}\text{Ar}/^{39}\text{Ar}$ cooling ages of detrital muscovite that was collected from small tributary catchments straddles the PT2 (Fig. 9.14C). North of the PT2, cooling ages average 10 Ma or less, whereas south of the PT2, cooling ages range from an average of 300 Ma to >1000 Ma. These data imply that the northern catchments have cooled at rates above 30°C/Myr, whereas the southern catchments experienced rates averaging below 1°C/Myr. This simplest, although not unique, explanation for the abrupt change in cooling ages is a previously unrecognized, surface-rupturing fault at the PT2.

Given that the cooling ages north of the PT2 imply rapid cooling since 10 Ma, the reader might justifiably wonder why this example is included under “intermediate time scales.” The reason is that erosion rates north of the PT2 are sufficiently high that many hundreds of meters of erosion would occur during 500 kyr and, as a consequence, the topographic indices examined here (hillslope gradients and channel steepness) would be sensitive to erosion of that magnitude.

Where terraces of different ages are preserved, patterns of deformation across tens to hundreds of thousands of years can be deduced, and sometimes constraints can be placed on the underlying fault geometry. Consider, for example, a suite of terraces in which progressively older terraces are increasingly back-tilted above a thrust fault (Fig. 9.15A). After subtracting the gradient of the modern channel, the magnitude of tilting can be defined, as well as a narrow zone in which each terrace transforms from tilted to simple planar uplift (Fig. 9.15B). Based on deformed terraces on New Zealand’s South Island, Amos *et al.* (2007) argued that this configuration of terrace deformation is most consistent with an underlying, near-surface listric thrust fault that transitions to a planar fault at depth (Fig. 9.15C). For this model, if the width of the tilted backlimb and its tilt magnitude, as well as the position and dip of the frontal fault, are known, then the radius of curvature of the listric fault, the magnitude of fault slip, the depth

to the transition to a planar fault, and the dip of the planar ramp can be calculated (Amos *et al.*, 2007). If the vertical offset (dz in Fig. 9.15C) of the non-tilted terrace treads is known, this offset provides a check of the dip prediction for the planar fault at depth. It is important to note, however, that listric faulting is not the only way to produce progressive terrace tilting: both detachment folding (Scharer *et al.*, 2006; Suppe *et al.*, 2004) and simple-shear fault-bend folding (Suppe *et al.*, 2004) can produce similar tilting. Sometimes the local geology can rule out alternative models, but commonly subsurface imaging is needed to test among them.

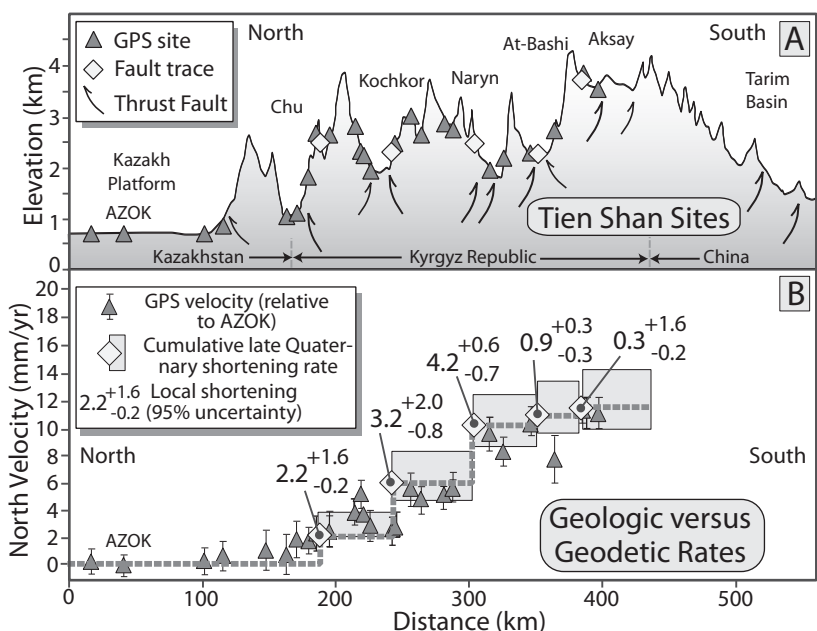
Fault-bend fold theory (Fig. 4.36A) (Suppe, 1983) predicts that, whenever a planar marker is transported through an active axial surface, the marker will deform in a geometrically predictable way. Consequently, planar geomorphic features, such as fluvial terraces, that are beveled or deposited across an active axial surface can be folded following the rules for fault-bend folds. This deformation is particularly obvious and useful on the backlimbs of folds where structural advection of a terrace through an active axial surface commonly forms a fold scarp (Fig. 9.16A and Plate 6). The dip of the fold scarp is a predictable function of (i) the dip of the original terrace surface and (ii) the angular difference in dip of the underlying fault plane on either side of axial surface (Hubert-Ferrari *et al.*, 2007; Chen *et al.*, 2007). From a tectonic perspective, the key aspect of the fold scarp is that its length approximates the slip on the fault since the terrace was created (Fig. 9.16B). Clearly, if the age of the terrace is known, then a fault slip rate can also be determined. Where multiple dated terraces are present, temporal changes in slip rates can also be assessed.

A spectacular example of a fold scarp was recently described by Hubert-Ferrari *et al.* (2007) from the southern margin of the Tien Shan in western China (Box 9.2). In this arid setting, erosional modification of many geomorphic features is modest, such that large triangular facets representing extensive remnants of fold scarps are well preserved in the landscape. In the cross-section at Quilitak fold (Fig. 9.17A), a remarkable, planar facet

Box 9.2 Geological versus geodetic rates of deformation.

The proliferation of GPS data on relative velocities across orogens and plate boundaries has provided a far more complete view of the modern patterns of crustal deformation. Although it is tempting to use these decadal rates as representative of rates applicable to hundreds of thousands of years, this equivalence has relatively rarely been tested. Along some well-studied strike-slip fault zones, such as the southern San Andreas Fault, where numerous paleoseismic studies define rates of slip on multiple faults at time scales of many thousands of years, geodetic and geological rates are quite closely matched.

Across contractional orogens, however, this match of rates is less clear. For example, in the Himalaya, geomorphic studies (Lavé and Avouac, 2000) clearly show that, at Holocene time scales, ~20 mm/yr of slip occurs at the Main Frontal Thrust (see Fig. 7.25). Yet, the geodetic shortening across the same zone is only a few millimeters per year. This large mismatch is interpreted to result from the presence of a locked megathrust, such that elastic strain is accumulating in the Greater Himalaya and is episodically released in large earthquakes that translate slip to the frontal thrust (Avouac, 2003). The Tien Shan, which span from China across Kyrgyzstan to Kazakhstan, are not underlain by a single megathrust, but instead comprise a series of fault-bounded ranges that are separated by narrow basins (see figure A). Recent earthquakes in the Tien Shan suggest that most fault planes dip quite steeply (~45°) and extend to depths of ~20 km (Ghose *et al.*, 1997, 1998), which is near the brittle–ductile transition. Hence, these faults are unlikely to be linked by a relatively shallow crustal detachment.



A. Topographic profile of the Tien Shan with major thrust faults, GPS sites, and studied fault indicated. B. Comparison of GPS north velocities with late Quaternary shortening rates. Modified after Thompson *et al.* (2002).

In an effort to define fault-slip rates across the Tien Shan, Thompson *et al.* (2002) analyzed numerous fold scarps, fault scarps, trenches across faults, and deformed terraces on major faults

within each of the Tien Shan basins. Most of the calibrated slip rates span the past 14–15 kyr (see Fig. 2.13), but some extend to >100 ka. One striking result of Thompson *et al.*'s study is that the cumulative geological rates, when plotted versus the geodetic data across the same area (Abdrakhmatov *et al.*, 1996), provide a good match to the geodetic rates (see figure B). This match suggests that, at least at time scales of several millennia, geodetic and geological rates are equivalent in the Tien Shan. This distributed deformation in the Tien Shan at geological time scales may be relevant for other orogens that comprise multiple fault-bounded ranges and lack an underlying megathrust. When Thompson *et al.*'s (2002) study was published, it was the first to provide calibrated slip rates across an entire contractional orogen that encompasses complex fault patterns.

stands ~700 m high. Based on a fault-bend fold model, the facet records ~1.1 km of slip (about equal to the length of the fold scarp) on the underlying thrust fault (Fig. 9.17B). Along strike on the Quilitak fold, multiple facets rise

to parallel linear ridge crests that display accordant heights and are nearly 4 km long (Fig. 9.17C and D). A surface fit to these ridge crests is interpreted to represent the uplifted erosion surface.

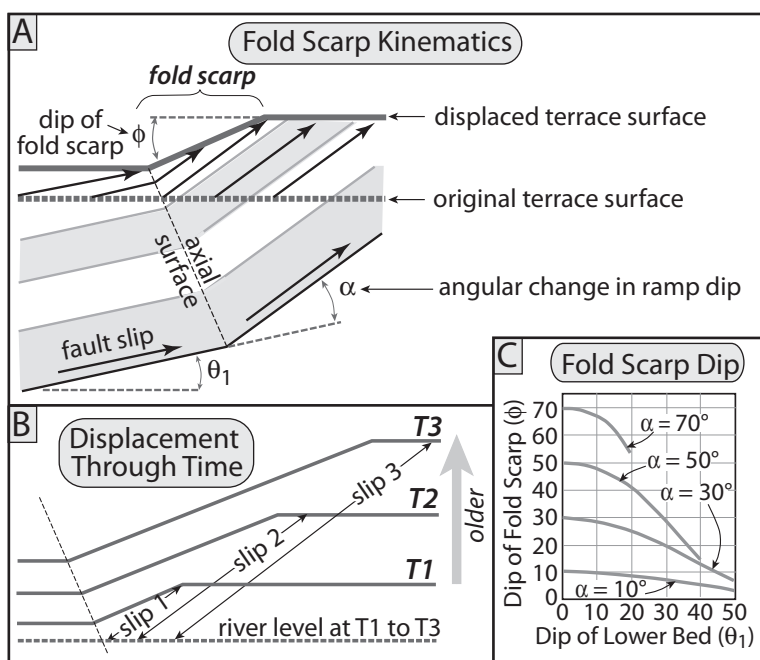


Fig. 9.16 Fold scarp kinematics and progressive terrace deformation.

A. Model for formation of a fold scarp in a fluvial terrace. The underlying fault has two planar segments that are separated by an active axial surface. Displacement is parallel to the underlying fault for material on either side of the axial surface (slip vectors). Terrace created at the dashed line will form a fold scarp whose length approximates (but underestimates) the fault slip since the terrace was formed. Modified after Thompson *et al.* (2002). B. Cartoon depicting three terraces that formed at different times at the same river height (dashed line). Length of the fold scarp approximates the slip for each terrace. Displacement pattern is based on the fault geometry of part A. C. Fold scarp dip (ϕ) as a function of the dip of the gentler dipping fault plane (θ_1) and the angle (α) between the fault planes on either side of the axial surface. Modified after Chen *et al.* (2007).

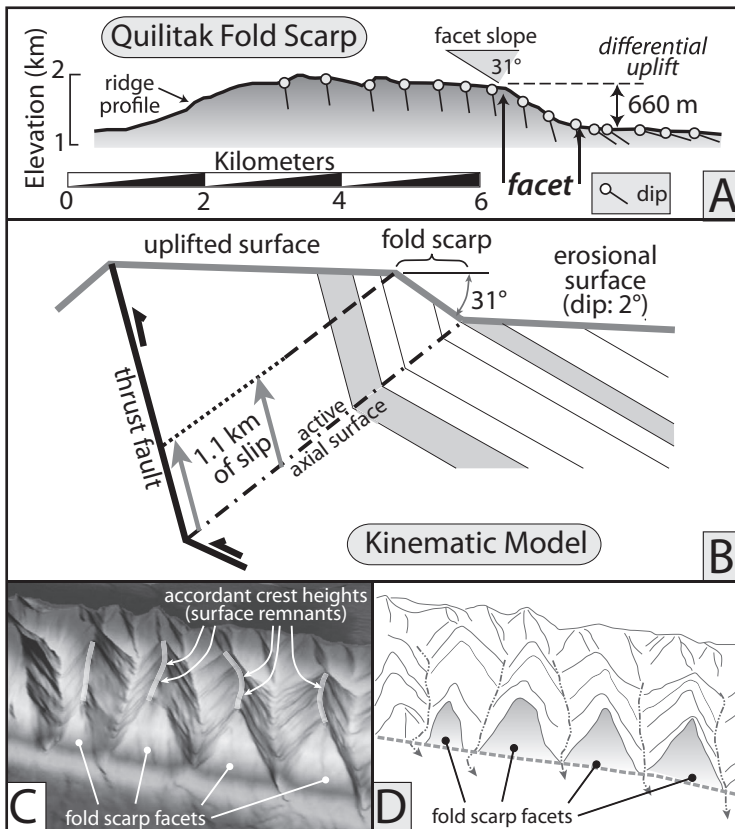


Fig. 9.17 Fold scarps in the southern Tien Shan.

A. Topographic profile and bedding dips along a ridge crest in Quilitak fold. Profile passes through a triangular facet with a dip of 31°, a height of 660 m, and a length of ~1 km. The facet is interpreted as a remnant of a fold scarp.

B. Formation of a fold scarp using a kinematic geometry that is consistent with the observed structure and geomorphology. C, D: Perspective views of fold-scarp facets and accordant ridge heights that define the approximate position of the uplifted strath or pediment. Modified after Hubert-Ferrari *et al.* (2007).

Given that Hubert-Ferrari *et al.*'s (2007) study suggests that the Quilitak fold has been deforming for several million years, why is the current morphology dominated by a single folded and moderately eroded paleoerosion surface? They suggest that, for most of Quilitak's growth, the sum of erosion of the fold plus sediment accumulation in the surrounding basin roughly balanced rock uplift, such that very little topography developed within the fold, despite its accommodating several kilometers of shortening. Within the past 200 kyr, however, they estimate that shortening rates across Quilitak increased about six- to eight-fold. As a consequence of this acceleration, the fold emerged as a prominent topographic entity that is dominated by the uplifted erosion surface that was present just prior to the accelerated growth (Hubert-Ferrari *et al.*, 2007).

In most sites of active folding, suites of deformed geomorphic markers that span a wide

age range are absent, such that the temporal evolution of the shape of a fold becomes difficult to discern. A tilted fold limb could have attained its current geometry by maintaining a constant dip and by lengthening through the toe of the fold or by lengthening through the fold's crest, or the limb could have rotated with a fixed length as in the listric fault model (Fig. 9.18A). Perhaps surprisingly, the long profiles of rivers incised into the fold limb may provide clues about the kinematic pathway of fold growth (Goode and Burbank, 2011). Under the assumption that channel incision rates are linearly proportional to stream power and that stream power is a function of upstream catchment area and channel slope, the temporal evolution of a river's long profile can be modeled as a function of the limb kinematics (Fig. 9.18B). A channel on a limb that is lengthening through its toe, for example, will always have an instantaneous incision rate that is maximized at its

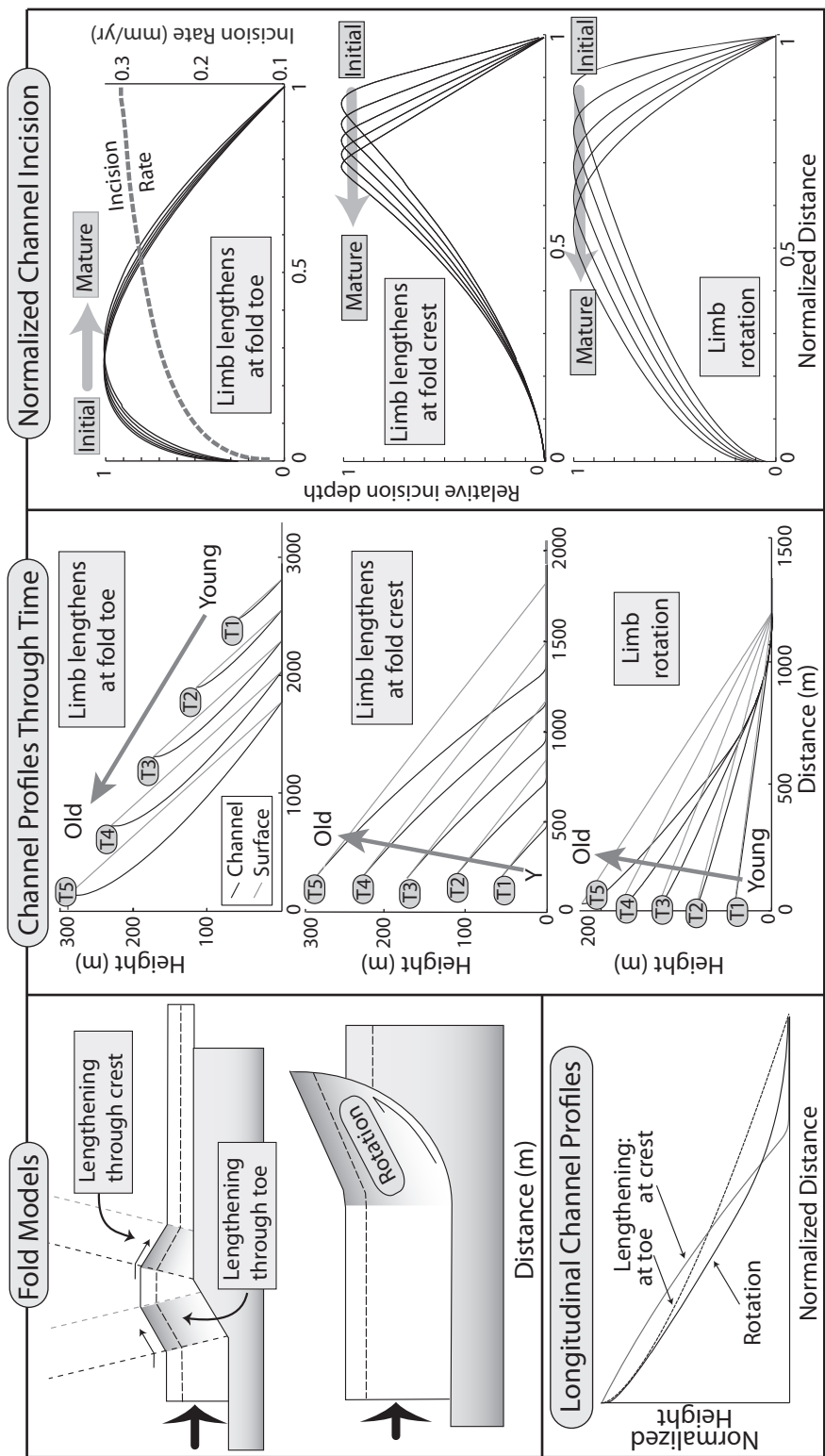


Fig. 9.18 Channel profiles on fold limbs for different fold models.

(Left, top) Different modes of limb growth: lengthening through the toe or crest at a constant angle, or rotation of a limb of constant length. (Center) River incision patterns through five time steps for different fold models. Both the pristine fold surface and the channel profile are depicted for each step. (Right) Spatial patterns of incision below an undissected surface for five time steps (as in part B). Note the migration of the point of deepest incision through time (arrows). Top figure also shows the instantaneous incision rate versus distance (dashed line). (Left, bottom) Normalized long profiles for each fold model at time step 5. Note the strong contrasts in concavity and overall shape. Modified after Goode and Burbank (2011).

toe. But, because pristine material continuously migrates through the axial surface at the toe and, thereby, adds new uneroded material to the base of the limb, the maximum amount of net incision occurs closer to the top of the fold (Fig. 9.18C). In contrast, a limb that is lengthening through the fold crest or that has a constant length but is steepening via rotation is predicted to have the most channel incision near the lower part of the fold limb. Whereas the boundary conditions for these models will certainly not all be matched by many field settings, the modeled patterns of incision provide a means to infer fold kinematics when other means may be lacking.

Transient landscapes

Because climate changes occur at rates that commonly outpace a landscape's tendency to reach equilibrium with the current climate, most landscapes are technically in a transient state all the time. Here, transient landscapes refer instead to landscape changes that occur, for example, in response to changes in the rate of base-level fall, rock uplift, or precipitation. Stepwise changes in any of these boundary conditions will force a landscape toward a new configuration. When a landscape is captured in this transitional interval, insights on both the nature and rates of change, as well as on key controlling variables, can commonly be obtained.

Knickpoints

Landscapes that are in transition from one state to another can provide insights on how surface and tectonic processes respond to changing boundary conditions. The migration of a knickpoint, a deceleration in the rate of rock uplift, a change in climate, or the growth of a fold, will each induce changes that will affect the rates of surface processes and ultimately modify the shape of the landscape. Such transitional landscapes commonly provide opportunities to examine landscape regions that have been affected by the change or ones that have not yet been affected. The contrasts between such areas

can serve to highlight the nature and rates of landscape change and perhaps can provide quantitative insights on controlling variables.

Consider the impact of a knickpoint on a trunk stream as it sweeps progressively upstream past numerous tributary channels. Each tributary will experience a relative drop in base level at the junction with the main stem. This drop is equivalent to increasing the rock uplift rate of the tributary catchment, such that we expect a knickpoint then to migrate up each tributary as well (Fig. 9.11). The Yellow River on the northern Tibetan Plateau provides a spectacular example of the impact of knickpoint migration on tributary channels and on rates of erosion (Harkins *et al.*, 2007). In the upstream end of the study area, the Yellow River progressively steepens, producing an upward convexity, as it descends ~900 m over the next 350 km (Fig. 9.19A). Two basins at the downstream end of the study area contain Plio–Pleistocene fills that rise ~600 m above the current level of the Yellow River. The tops of these fills are aligned and project upstream approximately to the level of the top of the modern Yellow River knickpoint (Fig. 9.19A). Along this projected gradient, several strath terraces are preserved, suggesting that the Yellow River previously flowed along this more even, gentler gradient. Recent magnetostratigraphic studies (Craddock *et al.*, 2010) show that the Tongde Basin was actively aggrading until ~0.5 Ma. Hence, if we assume that the accelerated incision of the Yellow River began at 0.5 Ma, the knickpoint migrated at a mean rate of ~50 cm/yr as it swept more than 250 km upstream! Along dozens of tributary channels, Harkins *et al.* (2007) used DEM analysis to document pronounced knickpoints that separate steep lower reaches from gentler upper reaches (Fig. 9.19B). In order to estimate the pre-knickpoint gradient of each tributary, Harkins *et al.* (2007) calculated the normalized steepness index, k_{sn} , (Eqn 9.2) for the river reach above the knickpoint. They then projected a channel with the same steepness downstream in order to estimate the former elevation of the tributary mouth (Fig. 9.19B). When the reconstructed elevations of the former mouths of numerous tributaries are plotted along the

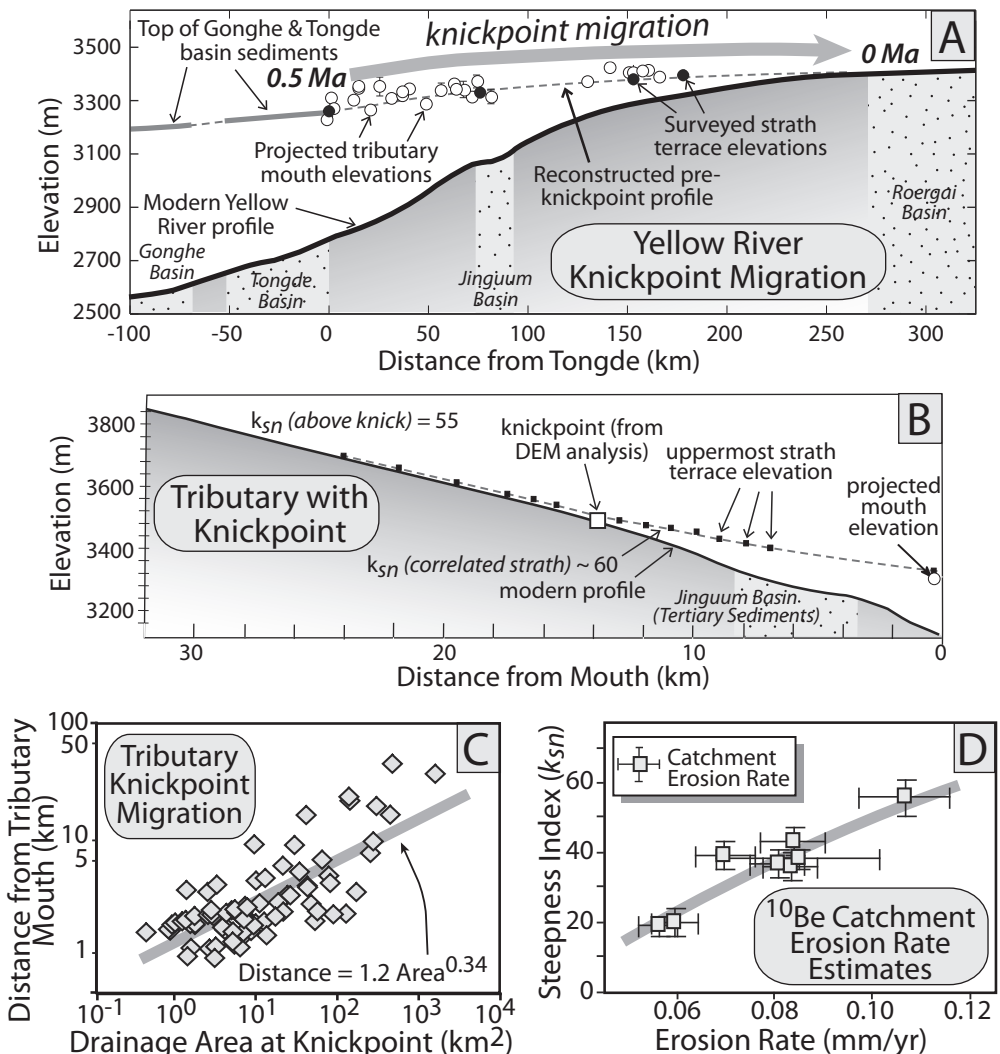


Fig. 9.19 Knickpoint migration along the Yellow River.

A. Long profile of the Yellow River, showing a pronounced knickpoint and the position of late Cenozoic basins. The tops of the downstream basins define a gradient that projects to the top of the knickpoint 250 km upstream. Along this gradient lie both preserved straths (black circles) and the projected former elevations of tributary mouths (open circles). B. Example of a tributary with a knickpoint ~14 km from the mouth. Observed normalized channel steepness above the knickpoint is used to project the pre-knickpoint channel gradient to the mouth (dashed line). Multiple strath terraces (small black squares) lie along this projected profile. C. The distance of the knickpoint from a tributary mouth scales with the drainage area upstream of the knickpoint. D. Catchment-wide erosion rates above knickpoints scale with the normalized steepness index. Modified after Harkins *et al.* (2007).

Yellow River, they align both with the observed straths and with the upstream projection from the downstream Gonghe and Tongde Basins to the top of the main-stem knickpoint (Fig. 9.19A).

Through their analysis of many dozens of tributaries, Harkins *et al.* (2007) developed an

extensive database with which to assess both proposed controls of knickpoint migration and landscape responses to falling local base level. For example, these data show a robust relationship between upstream drainage area and the distance each knickpoint has migrated

(Fig. 9.19C). Given that discharge is roughly proportional to catchment area, this relationship is consistent with observations from stream-table experiments in which migration rates scaled with discharge (Fig. 8.10A). This relationship further suggests that an erosion rule based on stream power can adequately describe the observed profiles. Harkins *et al.* (2007) also used detrital ^{10}Be concentrations in channel sediments upstream of knickpoints to determine catchment-wide erosion rates. Not only are these rates about an order of magnitude lower than incision rates below the knickpoints, but they also scale with the normalized steepness index, k_{sn} (Fig. 9.19D). Notably, most tributaries display a convex upward profile downstream of the knickpoint (Fig. 9.19B). This convexity suggests that these tributaries are still in a transient state of incomplete adjustment to their new base level. Note, for example, the contrast with the concave-up profiles above and below a knickpoint in a theoretical model for a migrating knickpoint (Fig. 9.11). Overall, this study of the Yellow River exemplifies the wealth of data and insights that can be gleaned from combinations of DEM analysis, chronological control on key events, calibrations of erosion rates, and both usage and tests of numerical models of rivers.

Pressure ridges

When strike-slip faults depart from verticality and when the fault trace bends into the path of the fault-slip vector, the resultant fault-normal stresses cause contraction and uplift, thereby forming a pressure ridge (Fig. 4.19). If the structural anomaly is persistently attached to a block on one side of the fault, the anomaly acts as a point source that drives uplift of the opposing block as it slides by. Once a given segment of the opposing block moves past the anomaly, uplift ceases. Thus, a very discrete spatial and temporal window exists in which the opposing block transitions, first, to experiencing the accelerated rock uplift and, second, to exiting the zone of uplift. The spatial extent of the window depends on the length of the structural anomaly parallel to the fault trace, whereas the pattern of uplift depends on the

subsurface shape of the structural anomaly. The temporal extent of the window depends on the fault slip rate and the anomaly's length. When a pressure ridge formed under these conditions can be identified, an illuminating opportunity exists to make a robust space-for-time (ergodic) substitution and to examine how the land surface responds to this transient pulse of uplift.

Along the San Andreas Fault in southern California, the Dragon's Back pressure ridge (Fig. 9.20) provides just such an opportunity (Hilley and Arrowsmith, 2008). Subsurface imaging at the Dragon's Back site (Unsworth *et al.*, 1999) defines a 2-km-long, structural knuckle attached to the North American Plate that juts beneath the Pacific Plate and drives rock uplift. The slip rate on the San Andreas Fault in this area is $\sim 33\text{ mm/yr}$ (Sieh and Jahns, 1984), such that each kilometer of Dragon's Back's length represents $\sim 30\text{ kyr}$. Recent acquisition of high-resolution (1-m pixel) lidar topography provides a high-resolution spatial database with which to quantify how the pressure ridge evolves in time and space as a geomorphic entity.

By mapping flat-lying rock formations that become uplifted in the pressure ridge, Hilley and Arrowsmith (2008) show that, over the first 2 km (to the southeast), the rock-uplift rate ranges as high as 2.3 mm/yr (Figs 9.20C and 9.21A). During the $\sim 70\text{ kyr}$ that it takes for any point on the Pacific block to pass across the structural anomaly, the total rock uplift is $\sim 80\text{ m}$ along the crest of the fold (Figs 9.20B and 9.21B).

Dragon's Back ridge is underlain by weakly consolidated Quaternary sediments that can be readily eroded. Consequently, the response time of various geomorphic processes to the tectonic forcing is expected to be quite rapid. For each drainage basin along the pressure ridge, Hilley and Arrowsmith (2008) measured several topographic metrics, including basin width and area, channel concavity and normalized steepness, relief within a radius of 50 m, density of landslide scars, and hillslope gradients. Their results show that local relief, normalized channel steepness, landslide density, and hillslope gradients all broadly track the uplift rate (Fig. 9.21). Despite the small size ($<0.5\text{ km}^2$) of the drainage

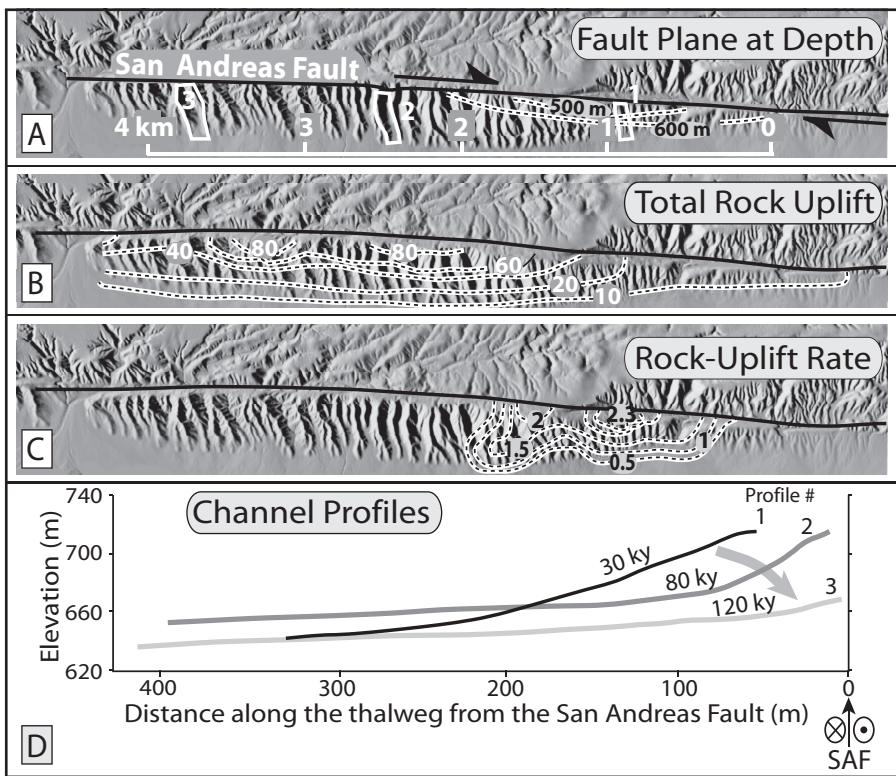


Fig. 9.20 Deformation patterns and channel profiles at Dragon's Back pressure ridge.

A. Shaded relief of Dragon's Back and the surrounding terrain. Note the leftward bend of the fault trend which drives compression. Contours indicate depth to the fault surface and show that the San Andreas Fault is offset in the subsurface toward the southwest. Numbers indicate channel locations in part D lidar DEM from www.opentopography.org. B. Total rock uplift within the pressure ridge. C. Rock uplift rate in mm/yr. D. Channel profiles for three catchments (shown in A). Ages are inferred based on the position of the basin along the pressure ridge and the assumed slip rate. Note the high concavity at 80 kyr and the much lower channel relief by 120 kyr. Modified after Hilley and Arrowsmith (2008).

basins that developed on the pressure ridge, channel and hillslope processes are shown to be intimately linked. For example, as uplift ceases, channel concavity abruptly increases (profile 2 at 80 kyr; Fig. 9.20D), thereby driving rapid channel incision. This incision undercuts adjacent hillslopes and, thereby, promotes increased rates of landsliding (Fig. 9.21E). Based on the space-for-time substitution, the response time of the channel is only ~ 7 kyr, whereas rates of landsliding only slowly diminish: more than 70 kyr is required to transition from hillslopes dominated by mass wasting to ones dominated by diffusive processes that typify the nearby landscape. This order-of-magnitude difference

in response times indicates a fundamental lag between channels versus hillslopes. Channels are the drivers that determine the rate of local base-level lowering and short-term rates of hillslope steepening; hillslope processes then respond to that steepening.

For Hilley and Arrowsmith's (2008) study, the combination of high-resolution topography, superb time control, and a well-constrained structural setting underpins their ability to closely examine both the pattern of tectonic forcing and the diverse geomorphic responses to this forcing. Investigations of different, but similarly well-constrained, tectonic settings, as well as analogous settings but with contrasting

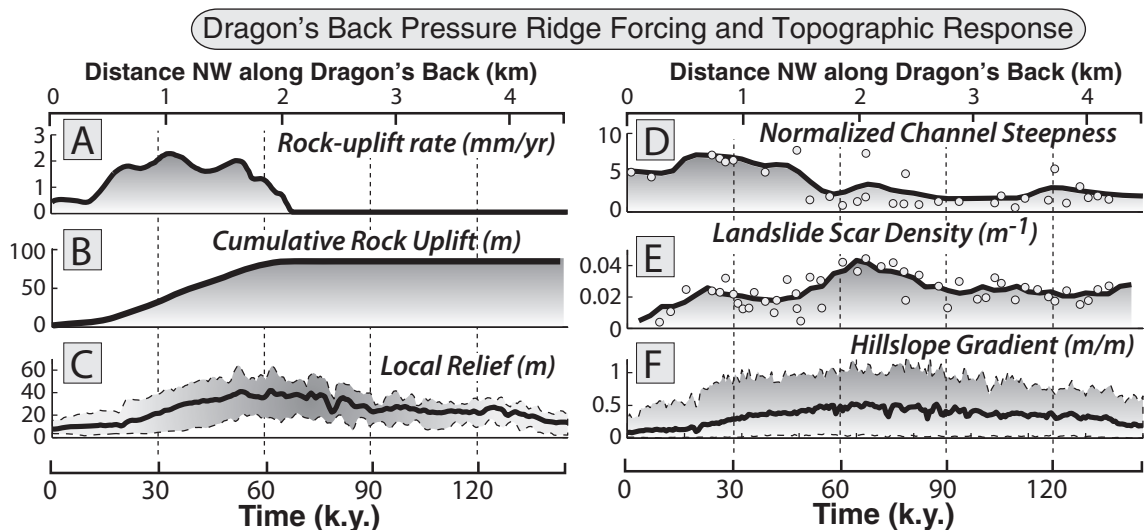


Fig. 9.21 Rock uplift and geomorphic metrics at Dragon's Back pressure ridge.

Distance is measured toward the northwest and starts at the inception of uplift. Time is based on an assumed San Andreas slip rate of 33 mm/yr or 1 km in 30 kyr. Topographic data were extracted from a 1-m DEM.

A. Rock-uplift rate along the crest of the pressure ridge. B. Cumulative rock uplift along the crest. C. Local topographic relief measured in a 50 m radius: average relief (solid line) and 95% bounds (shaded area). D. Normalized channel steepness based on a reference concavity of 0.68 (mean of the entire data set). Only catchments for which a linear log-area-slope trend could be identified that spanned more than an order of magnitude of catchment area were included. E. Landslide scar density. F. Hillslope gradients. Modified after Hilley and Arrowsmith (2008).

climate, lithology, or vegetation, promise to shed more insight on tectonic-geomorphic linkages.

Growing folds

Whether they are laterally propagating or have rather fixed tips, growing folds represent a special type of transient landscape, because, along their length, progressive changes occur in their geometric attributes, such as the magnitude of differential uplift or the slope of their limbs. Perhaps most importantly, laterally propagating folds can provide a robust space-for-time substitution, and, when the ages of uplifting surfaces are known, rates of processes can be defined.

As described previously, as faults accumulate displacement, they commonly increase the size and length of their rupture surface. The plunging noses of hanging-wall anticlines and footwall synclines that develop in conjunction with either emergent or blind thrusts would, therefore, be expected to propagate laterally as

the tip of the underlying fault migrated with each successive rupture event. Simultaneously, especially in the early stages of development, these growing folds progressively increase in amplitude and breadth with each successive earthquake. As their flanks rise above local base level, they are attacked by erosional surface processes, and their pristine surfaces begin to be modified. Meanwhile, as their noses propagate laterally, the resultant uplift influences the gradients and geometries of nearby fluvial systems. Thus, two rather different responses to growing folds are potentially recorded in the geomorphological record: in one, the shape of the fold is modified by surface processes; in the other, the actual growth of the fold modifies the surface processes (Keller *et al.*, 1999). The degree of surface modification may be an indication of the age of various parts of a fold and the local rate of deformation, whereas river patterns with respect to the fold may reveal their interactions over time. Analysis of these interactions can

provide insights on a history of fold growth that are otherwise unattainable (Burbank *et al.*, 1996c, 1999; Keller *et al.*, 1998). Several key data sets can contribute to such a history, including: topographic data on the fold crests, limbs, and nose; dates on geomorphic surfaces and features along the fold; detailed analysis of the underlying structural geometry; and variations of structure along the length of the fold.

Consider first the ways in which a fluvial system that was previously flowing across a relatively low-relief landscape may interact with a growing fold or a suite of growing folds. For any individual fold, as it emerges above the adjacent land, a new drainage divide is defined along the fold crest and new catchments are formed along its flanks: it subdivides formerly continuous drainage systems, and the new catchment configuration is closely tied to the fold geometry. Asymmetrical folds with steep forelimbs will have short, steep catchments on their forelimbs and elongate, gentler catchments on their backlimbs. This asymmetry is readily visible in map patterns of river courses (Talling and Sowter, 1999; Talling *et al.*, 1997).

Streams that had formerly flowed across the site of the growing fold either (i) are diverted parallel to the fold axis and around the nose of the fold, (ii) become entrenched as antecedent streams that incise across the uplifting fold, or (iii) bevel off the top of the emerging fold so that it has little or no topographic expression. In order to maintain its course through a water gap across a rising fold, an antecedent stream must maintain a basinward-dipping gradient across the fold. Otherwise, the stream will be diverted along the upstream margin of the fold. A folding event will cause relative uplift of the channel reach within the folding domain (Fig. 9.22A), causing a likely instantaneous reversal of the channel gradient immediately upstream of the fold. Sediment will tend to be ponded in this depression and begin to fill it. At the same time, a knickpoint will begin to propagate upstream from the newly steepened zone on the downstream end of the uplifted reach (Fig. 9.22B). A competition, therefore, exists between the rate of differential rock uplift in the fold and the rate of aggradation upstream of the fold.

If the sediment load of an antecedent stream is insufficient to aggrade as fast as the fold is rising, the stream is likely to be diverted (Humphrey and Konrad, 2000). Several other factors can affect whether a channel can sustain its course. First, if a layer of alluvium that is a few meters thick is part of the longer-term transport load of the channel floor, then, in response to uplift that is less than the thickness of the alluvium, the channel will simply incise its bed rapidly through the alluvium and sustain its course. Second, if rock strength is low across the core of the fold, then a knickpoint will more rapidly propagate from the downstream to the upstream end of the uplift and, thereby, restore a downstream gradient. Third, as the fold widens during continued growth (Fig. 9.22C), the gradient of antecedent channels across the fold will decrease and cause a concomitant decrease in the erosive power of the stream (Burbank *et al.*, 1996c). Whereas the first two conditions promote maintenance of an antecedent channel, the last condition promotes its diversion.

When analyzing the map pattern of stream valleys associated with growing, laterally propagating folds, the expectation should be that a series of wind gaps along the fold crest will record the progressive defeat of older, antecedent streams and that, where a stream is still antecedent, the fold has not broadened and uplifted sufficiently to defeat the stream. As successive antecedent streams are defeated, the remaining streams will capture the discharge of the defeated streams and will augment their discharge (and probably stream power) as they cross the anticlinal crest. Thus, the most likely location for an antecedent stream is near the propagating nose of a fold (Burbank *et al.*, 1996c; Jackson *et al.*, 1996).

An illustrative example of both antecedent and diverted channels is well displayed in the southern Tien Shan of western China (Hubert-Ferrari *et al.*, 2007). Here, as deformation encroaches on the adjacent foreland, a new, elongate fold that is 200–300 m high has grown in front of an older fold that is cut by antecedent streams. Prior to the growth of the new fold, those antecedent streams fed alluvial fans about 10 km long whose apices lay on the downstream

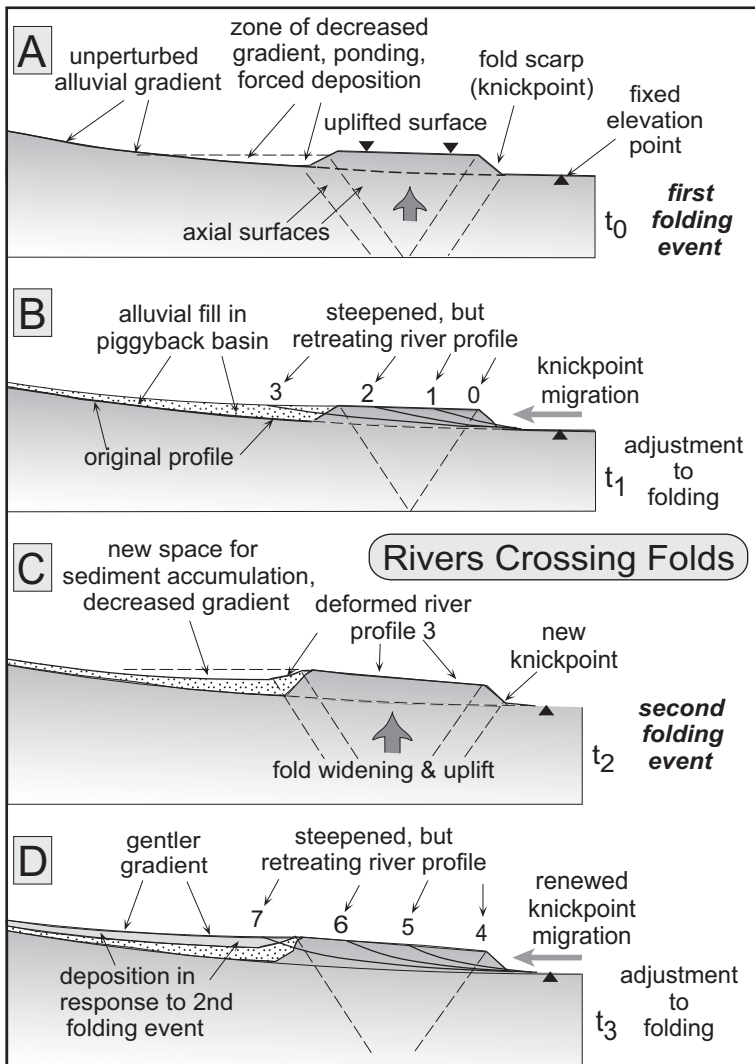


Fig. 9.22 Interactions of an antecedent stream with a growing fold.

Fold uplift creates accommodation space for sediment in the piggyback basin. Deposition in the piggyback basin allows the stream gradient to steepen across the fold, but also raises the river above the surrounding plain. Such deposition promotes avulsion, often away from the former water gap. With each increment of uplift, a knickpoint forms at the downstream end of the fold and propagates upstream. Modified from Burbank *et al.* (1996c).

edge of the older fold (Fig. 9.23). As is typical with fans, a suite of radial channels emanated from each fan apex. During growth of the new fold, most of these channels were defeated, leaving elongate linear valleys and numerous wind gaps that now decorate the fan crest. Owing both to the lateral continuity of the new fold and to the fact that most of the modern fans have beveled laterally several kilometers into the upstream flank of the fold, most defeated streams do not appear to have been diverted around the fold tip. Instead, a few of the antecedent channels have

gathered the flow from defeated ones and sustained their courses across the new fold (Fig. 9.23). The relationships between the fans, channels, and the new fold change along strike. Beyond the fold tip, the lateral extents of the old and modern fans are the same. At the tip, the modern fan margin has been deflected ~5 km away from the tip. Farther along the continuous fold, modern fans have radii that are 3–5 km shorter than the older fans that preceded them. The piggyback basin is aggrading with fan sediments and, depending on that rate of aggradation

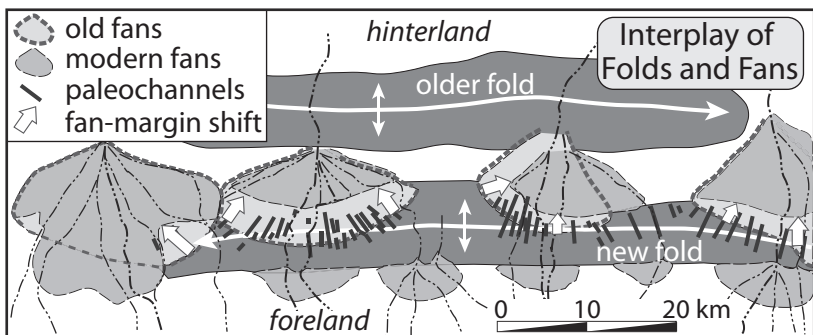


Fig. 9.23 Growing folds, antecedent rivers, and abandoned paleochannels.

Interactions of an older and younger fold with drainage systems in the southern Tien Shan. The older fold is the Quilitak fold previously described (Fig. 9.17). North of the newly emergent fold, fan margins have retreated, whereas along the new fold's crest, abandoned paleochannels record the radial drainages of alluvial fans that pre-date the younger fold. Only a few of the paleochannels persist as modern antecedent streams. Modified after Hubert-Ferrari *et al.* (2007).

versus the rate of tip propagation and vertical fold growth, more of the channel flow may someday be diverted around the new fold's nose.

In order to determine rates of deformation and geomorphological modification of growing folds, dates are needed to define when the fold propagated into a given position and how rapidly it grew vertically and laterally. One such dated structure is Wheeler Ridge anticline near the southern end of the San Joaquin Valley of California (Fig. 4.39). Because Wheeler Ridge encompasses an actively producing oil field, numerous wells with accompanying electric logs provide a basis for correlation among the wells, help to define the stratigraphic boundaries in the subsurface, and serve to delineate the overall structure (Medwedeff, 1992). The anticline is strongly asymmetric, with a relatively steep ($\sim 45^\circ$) forelimb and much gentler (17°) backlimb. The fault geometry underlying the anticline has been interpreted as a wedge thrust (Fig. 9.24). The Wheeler Ridge anticline plunges to the east and dies in an actively aggrading alluvial plain. From the fold tip, the differential uplift gradient is $\sim 200\text{ m/km}$ across the easternmost 3 km of the anticline (Fig. 9.25) (Medwedeff, 1992). The topographic relief of the fold is considerably less than the structural uplift, because synfolding aggradation has raised the surface of the surrounding depositional basin.

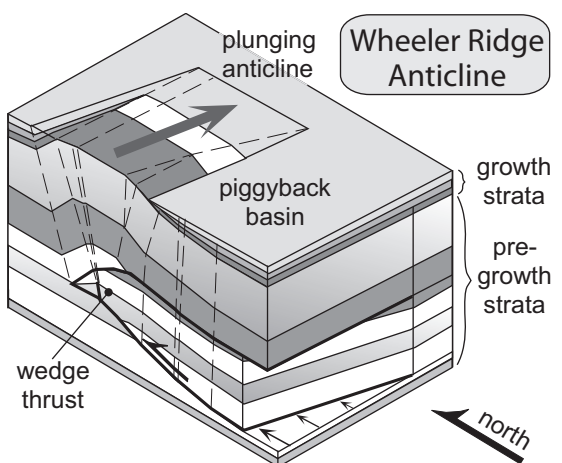


Fig. 9.24 Block diagram of structure of Wheeler Ridge. Structural interpretation of a wedge thrust with the anticline being underlain by a north-vergent thrust fault and a passive roof thrust. Displacement and uplift decline eastwards. Modified after Medwedeff (1992).

As the fold propagates, formerly actively aggrading surfaces adjacent to the fold are uplifted and incorporated into it. Following initial uplift, these surfaces accumulate few new sediments (except some loess) along the crest of the fold. If the timing of the end of active alluvial deposition or the age of the soil that developed on the uplifted surface can be determined at several points along the fold, these

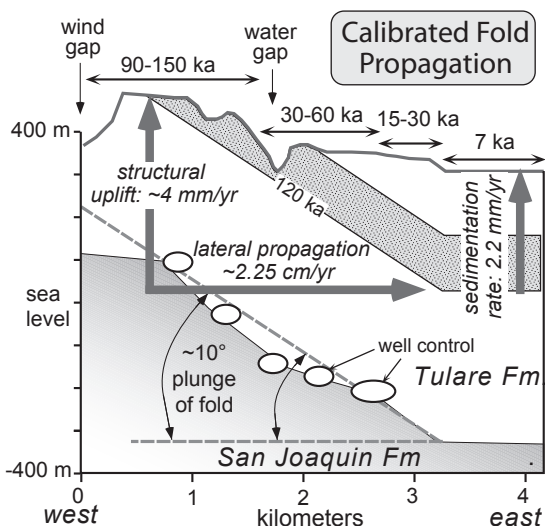


Fig. 9.25 Calibrated rates of fold propagation, crestral uplift, and sediment aggradation for Wheeler Ridge.

Schematic cross-section along the plunging axis of Wheeler Ridge anticline, showing ages, relief, and propagation rates based on well data. Note the importance of surface ages for defining the rates of uplift, propagation, and sedimentation. Modified after Medwedeff (1992).

ages will constrain the initiation of fold growth at those points. Based on soil stratigraphy and both radiocarbon and uranium-series dates at Wheeler Ridge (Fig. 9.25), the youngest uplifted area at the emergent eastern end of the anticline is dated at about 7 ka, whereas the alluvial surfaces just east of the wind gap are estimated to date from 90–150 ka (Keller *et al.*, 1998; Medwedeff, 1992; Zepeda, 1993). When combined with the structural and stratigraphic data, the ages indicate that, during the past 100 kyr, sediment accumulated in the adjacent basin at a rate of about 2 mm/yr, and the crest of the fold uplifted at a rate of about 4 mm/yr, while the nose of the fold propagated eastward at a rate of about 25 mm/yr.

If one were to assume that a significant earthquake occurs on the underlying fault once every 400 years, these rates imply that, with each rupture, the fold crest would be uplifted approximately 1–2 m, and the fault would extend its eastern tip about 10 m. The rates of growth of

the vast majority of folds identified within the entire geological record are essentially unknown. By developing a chronology that spans 100 kyr, these dates at Wheeler Ridge provide unique insights on the mean rates of anticlinal growth and facilitate development of more detailed and reliable kinematic models of fold growth and geomorphic dissection.

The drainage geometry and topography in the vicinity of Wheeler Ridge reveal interactions between fold growth and river responses (Figs 4.39 and 9.25). Whereas the floor of the wind gap has been uplifted ~100 m above the expected fluvial gradient across the current fold, the crest of the fold lies 300 m above the floor of the paleovalley. Hence, an antecedent river had successfully incised across the fold during about three-fourths of its vertical growth. An asymmetric catchment funnels runoff from near the current wind gap to the present water gap (Fig. 4.39). This asymmetry suggests the direction of fold propagation and river diversion. At the current water gap, the fold is narrower than at the wind gap and the upstream catchment is larger, such that the discharge and potential stream power (dependent on channel slope) would also be greater. Given the approximately 200 m of relief bounding the water gap (Figs 4.39 and 9.25), it, too, has persisted for a considerable interval of fold growth. Drainage on the fan to the east of the fold swings around the fold nose and converges toward the northwest, where finer-grained sediment accumulates in a depositional “shadow zone” in the lee of Wheeler Ridge (Fig. 4.39B).

In the context of the reconstructed history of fold growth, the geomorphic responses to folding and the modification of the fold by surface processes can also be examined in more detail than is commonly possible. The apparently systematic eastward propagation of the Wheeler Ridge anticline permits the ergodic hypothesis to be applied. Visual inspection of Wheeler Ridge (Fig. 4.39A) clearly shows significant changes in the character of the land surface along the length of the fold. Initially, as the nose of the fold propagates eastward, a planar region of the alluvial surface is uplifted and gently folded. At this point, the geomorphic surface should precisely mimic the structural geometry

Table 9.1 Effects of slope steepening and lengthening on geomorphology and surface processes.

Feature/process	Effect of steepening and slope lengthening	Reason behind effect
head of first-order streams	channels begin higher upslope	channel initiation is function of $(\text{slope} \times \text{area})$
ruggedness (mean relief \times drainage density)	increases with steepening and lengthening	more first-order channels lower on slope and deeper channels to match relative base level
creep and landslides	increases with steepening and lengthening	shear stress is a function of slope: $\sigma = \rho gh \sin \alpha$
exported material	increases with steepening and lengthening	flux proportional to slope (dy/dx)
balance of uplift versus incision	uplift tends to outpace incision for antecedent streams	width of structure increases with time; discharge stays constant, but river slope and mean stream power decrease

of folding. Following uplift, however, surface processes begin to modify the surface in several ways. Channel heads appear on slopes exceeding about 5° (Keller *et al.*, 1998; Talling and Sowter, 1999). Antecedent streams incise into the growing fold and, in the particular situation at Wheeler Ridge, are commonly localized by transverse tear faults (Mueller and Talling, 1997). As gullies deepen, the pristine, but uplifted, alluvial surface becomes more dissected, and landsliding begins to occur on the sides of the larger gullies. As the steep forelimb lengthens, creep and shallow landsliding become increasingly important, and gullies extend their heads toward the crest of the fold. If fold widening and vertical uplift are sufficiently rapid, antecedent streams are defeated and diverted, leaving behind wind gaps (Fig. 4.39A).

Modification of the fold's geomorphic surface can be analyzed from at least two perspectives: changes along the length of the anticline; and contrasts between the forelimb and the backlimb. The western parts of the anticline are older, have greater topographic relief, and commonly are steeper than the younger, eastern parts of the structure. In any transverse cross-section of this fold, the forelimb is consistently steeper than the backlimb (Fig. 9.24). All slope-dependent processes would, therefore, be expected to attack the forelimb more vigorously than the backlimb. Similarly, catchment areas, discharge, and relief generally increase toward the west. The net results are that the fold becomes

increasingly dissected toward the west and that the forelimb is more dissected than the backlimb along any transverse section. Qualitative predictions of changes along the fold (Table 9.1) suggest how various surface processes will be influenced by the growing relief and both lengthening and steepening of the fold limbs.

Analysis of a 30-m digital elevation model (DEM) of Wheeler Ridge permits further quantification of several aspects of the geomorphology. Slopes and relief were calculated within a sliding 150 × 150 m window along the fold limbs, excluding the wind and water gaps (Brozović *et al.*, 1995) (Fig. 9.26). The resulting distributions show that both slope and relief (Fig. 9.26) are consistently higher (i) on the forelimb than on the backlimb and (ii) in the older parts of the fold. These data support the hypothesis that the enhancement of slope-dependent processes promotes greater dissection of the fold limbs (Table 9.1).

As shown earlier (Fig. 7.6), digital topography can also be used to calculate minimum volumes of eroded material along an anticline. At Wheeler Ridge, the pre-dissection topographic surface can be reconstructed by connecting undissected remnants of the uplifted surface of the fold. Subtraction of the current topography from that pre-dissection surface defines the magnitude of erosion throughout the fold (Plate 8). These calculations indicate that the most extensive erosion has occurred in the older, more strongly uplifted segments of the fold, whereas very little erosion

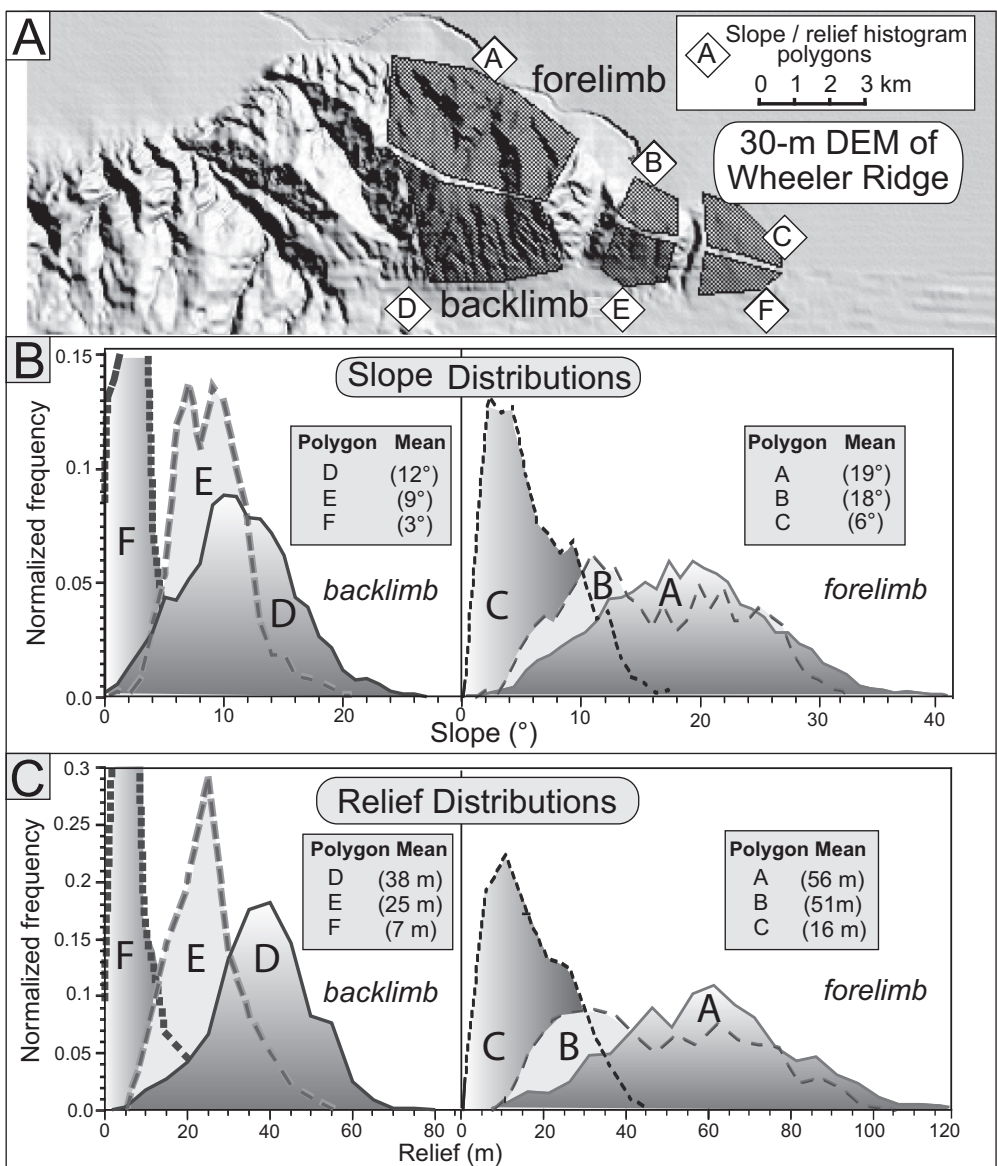


Fig. 9.26 Wheeler Ridge geomorphology.

A. Polygonal areas represent calculation areas on either flank of the Wheeler Ridge anticline. Magnitude of rock uplift and dissection increase toward the west. B. Slope distributions (150×150 m window) for polygons shown above. Note progressive changes from old (A) to young (C) and the persistent difference between the forelimb (A-C) and backlimb (D-F). C. Relief distributions for the same polygons. Modified after Brozović *et al.* (1995).

has occurred near the eastern nose of the fold. The magnitude of erosion (eroded volume/source-area size) is always higher on the forelimb rather than the backlimb (Fig. 9.27A); this contrast supports the concept of erosion rates

being slope dependent. The rates are also higher on the older parts of the fold, where greater relief is present and more time for dissection has elapsed (Fig. 9.26). A plot of the rates of dissection versus the mean slope (Fig. 9.27A) shows

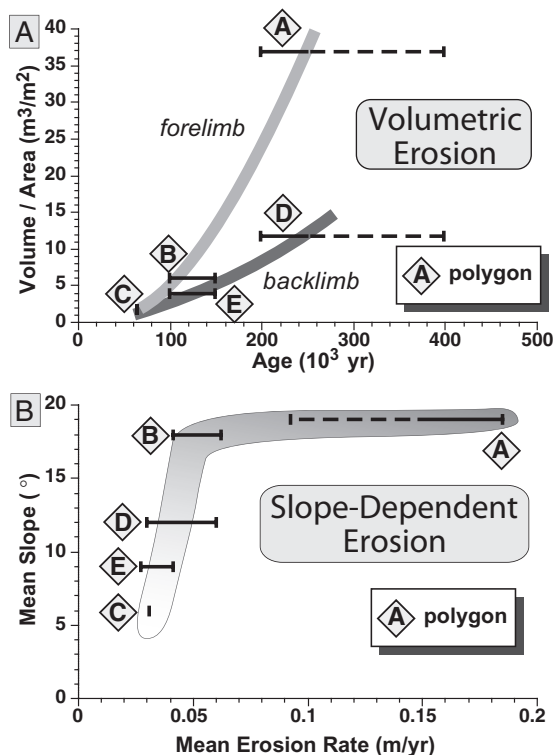


Fig. 9.27 Quantified erosion on Wheeler Ridge anticline.

A. Eroded volume per unit area plotted versus the age of the dissected surface. Note increasing rates with age and persistently higher rates on the forelimb for each age grouping. Polygons are the same as those shown in Fig. 9.26. B. Mean erosion rate versus slope angle in each polygon. Modified after Brozović *et al.* (1995).

predictable increases in rates for increasingly steep slopes. The abrupt increase in erosion rate for slopes $>17^\circ$ probably does not indicate some threshold slope angle, but rather that the longer slopes, greater relief, and more areally extensive gully headwalls in the older part of the fold have promoted more rapid erosion there.

This analysis of Wheeler Ridge highlights some of the ways in which ages on uplifted surfaces, recognition of structural geometries and geomorphic patterns, and quantification using digital topography can be used to develop a fuller understanding of the rates of fold growth and dissection over thousands of years. If combined with field measurements

of geomorphic processes and with paleoseismic analysis, it may be possible to develop more realistic models of fold development and erosional modification that span from decades to many thousands of years.

The fault-bend fold developed above the Main Frontal Thrust in central Nepal (Fig. 7.25C) provides a well-calibrated setting for examining how rocks that experience rapid lateral advection ($\sim 20\text{ mm/yr}$) are eroded as they are uplifted. One intriguing prediction is that topographic features can also be advected across a fold (Miller and Slingerland, 2006; Miller *et al.*, 2007). Observations that support this prediction include the fact that a high proportion of valleys and saddles in the topography are aligned from one side of the fold to the other across the fold crest (Fig. 9.28A and B). This alignment suggests that northward-draining river valleys that formed on the hinterland flank of the fold are advected across the fold crest and become southward-draining valleys on the distal (foreland) flank. Numerical modeling of landscape evolution in the context of rapid lateral advection of rocks (Miller and Slingerland, 2006; Miller *et al.*, 2007) predicts that such alignment of valleys should be common for major topographic elements, such as ridges and valleys, when advection rates are rapid compared to erosion rates (Fig. 9.28C and D). Whereas topographic advection on these frontal folds is predicted to occur at scales of a few kilometers and $\sim 10^5$ years, larger features such as deep river gorges may also be advected at longer time scales (Koons, 1995).

Fault behavior

Propagating versus fixed faults

Age-calibrated data on displacement profiles gathered at intermediate scales can serve to discriminate between faults whose tips are propagating and those whose tips are fixed (Fig. 9.29). In a broad sense, the shape of the overlying fold might show little difference as a function of whether the fault tips are fixed or propagating (Fig. 9.1), although fixed-tip folds are expected to have steeper displacement gradients near their tips than do steadily

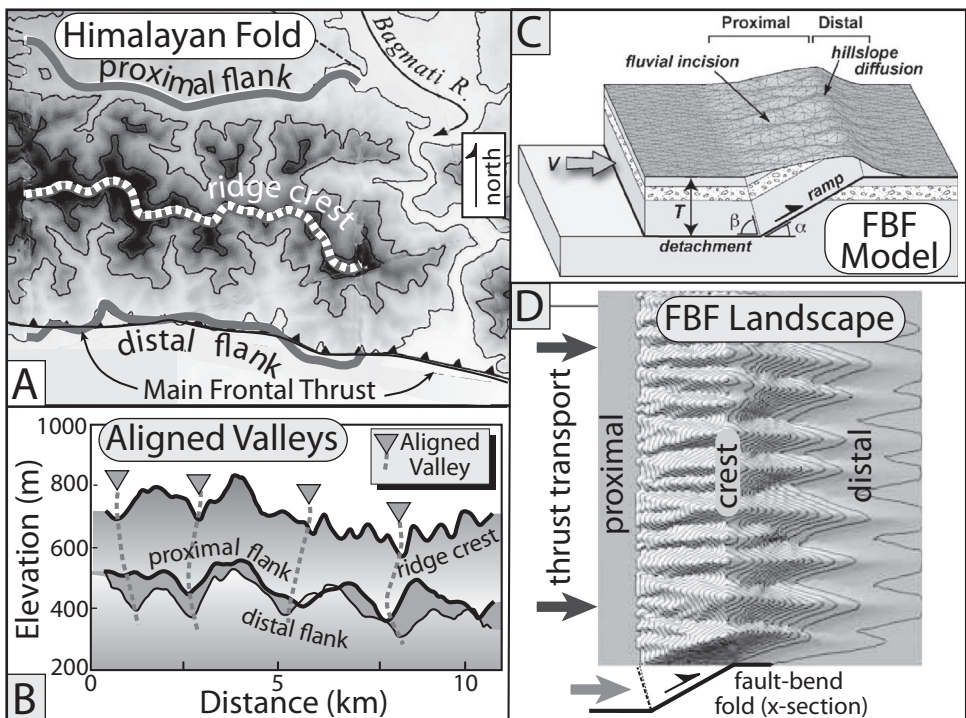


Fig. 9.28 Topographic advection on fault-bend folds.

A. Contour map of topography on a fault-bend fold developed above the Main Frontal Thrust in central Nepal (see Fig. 8.21 for cross-section). Lines along the crest and the distal and proximal flanks depict the location of topographic profiles in B. B. Topographic profiles show an overall alignment of major valleys on both fold flanks and the ridge crest. C. Set-up for numerical model of eroding topography above a rapidly advecting fault-bend fold (FBF). D. Map view of predicted model topography depicting clear valley alignment on either flank of the fold. Cross-section at bottom shows relationship of kinks in the fault surface to the topography. Modified after Miller and Slingerland (2006) and Miller *et al.* (2007).

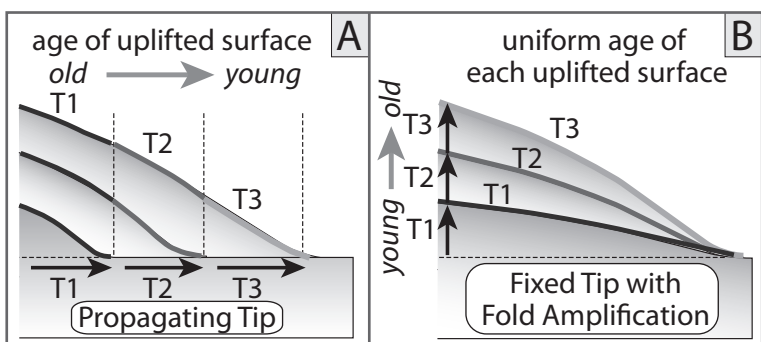


Fig. 9.29 Propagating versus fixed-tip folds.

A. Propagating fold tip in which the geomorphic surface beyond the fold tip is progressively incorporated into the propagating tip, causing surface ages to get younger toward the tip. T1 to T3 represent both time increments of fold growth and surface ages along the fold's crest. B. Fixed-tip fold in which continued displacement leads to amplification of the fold. The upper surface has the same age, irrespective of position with respect to the tip.

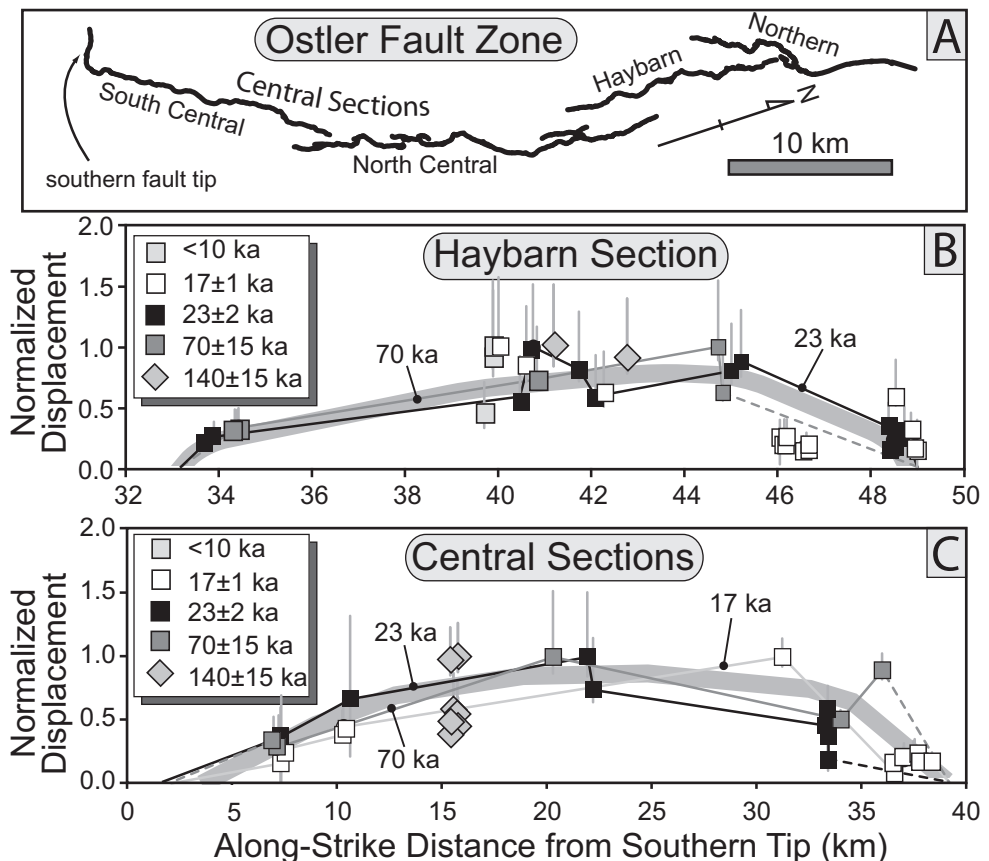


Fig. 9.30 Fixed-tip faults in the Ostler Fault zone.

A. Map of the surface trace of the Ostler Fault, an east-vergent thrust fault. Normalized displacement versus length on the Haybarn (B) and Central (C) sections. Similarities of the normalized profiles at 17, 23, and 70 ka argue for fixed tips on each of these segments. Modified after Amos *et al.* (2010).

propagating folds (Fig. 4.10). The use of normalized displacement gradients and of ages of geomorphic surfaces can permit unambiguous discrimination among these fault-growth models. For a fold whose tip is propagating, ages along the upper surface of the fold should get progressively younger toward the tip (Fig. 9.29A). In contrast, two diagnostic features help distinguish fixed-tip folds. First, deformed geomorphic surfaces should have the same age along their length (Fig. 9.29B). Second, normalized length-displacement profiles should remain similar irrespective of age, i.e., ongoing differential uplift amplifies the fold in a self-similar way.

Given the progression of ages along its crest, Wheeler Ridge anticline provides an excellent

example of a propagating fold (Fig. 9.25). In contrast, a succession of deformed and dated terraces along the Ostler Fault in New Zealand suggests that the tips of current fault segments have been fixed for many millennia (Fig. 9.30). A suite of fluvial terraces ranging in age from Holocene to the penultimate glaciation (140 ka) have been deformed along the length of the Ostler Fault (Amos *et al.*, 2010). Although older terraces have been significantly more deformed than younger terraces, the patterns of normalized displacement versus length appear indistinguishable from one terrace to the next, despite a seven-fold range of ages (Fig. 9.30B and C). This similarity in shape and the absence of lengthening of the fault

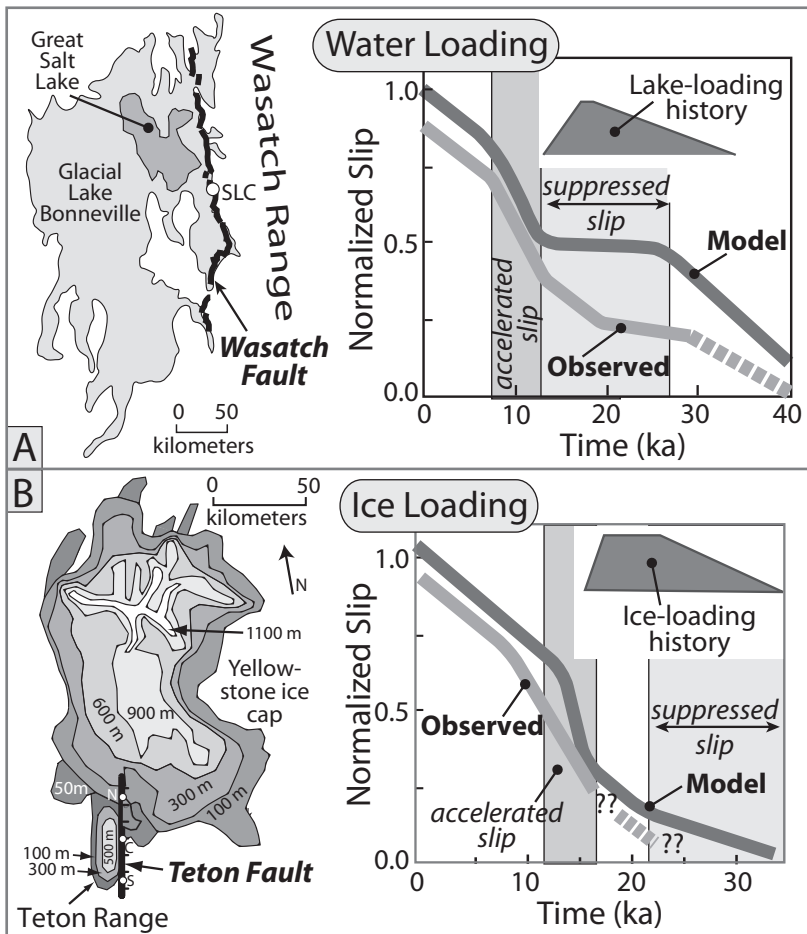


Fig. 9.31 Climatic modulation of fault slip rates.

A. Water loading. (Left) Areal extent of glacial Lake Bonneville in proximity to the Wasatch Fault. (Right) Numerical model of normalized slip and slip-rate changes in response to lake-loading history that extends from 34 to 13 ka (dark trapezoid) in comparison to observed slip (see Fig. 6.30). Note that the model predicts a prolonged interval of suppressed slip when the lake is present, followed by brief, but significantly accelerated, slip rates when the lake load is removed. B. Ice loading. (Left) Reconstructed ice thickness for the Yellowstone ice cap and the Teton Range. (Right) Modeled slip history of the Teton Fault in response to the waxing and waning ice load compared to the fault's observed slip history. Note that the observed history only extends to ~16 ka. Modified after Hampel *et al.* (2007) and Hetzel and Hampel (2006).

provide strong evidence for a fixed fault tip, at least for the past 140 kyr.

Climatically modulated fault slip

The observed temporal coincidence of summertime water loading in the Himalayan foreland and suppression of both seismicity and convergence rates in the hinterland suggest climate-tectonic linkages at seasonal time scales (Box 5.2). Uncertainty remains, however, about whether variations in loads at intermediate time scales also impact rates of deformation. From a theoretical perspective, we expect that changing water, ice, or rock loads could influence fault behavior (Fig. 9.2), and several recent studies provide data supportive of such linkages. In each

case, climate change has induced the expansion and subsequent contraction of either a large lake or an ice cap during late Quaternary times. Whereas the growing load of the lake or glacier is predicted to have moved nearby normal faults farther from failure and, thereby, to have reduced their slip rates, waning ice or water loading should have caused accelerated slip rates (Fig. 9.2). For example, at its maximum extent at ~18 ka, glacial Lake Bonneville covered more than 50 000 km² (Fig. 9.31A) and was over 300 m deep (Gilbert, 1890). During most of Lake Bonneville's existence, numerical models predict that slip rates on the nearby Wasatch Fault should be suppressed (Hetzel and Hampel, 2006). As the lake shrank at ~12.5 ka, slip rates are predicted to have rapidly accelerated for several thousand

years. Although the observed slip history on the Wasatch Fault (Fig. 6.30) does not perfectly match the modeled slip-rate changes, the shape of the observed curve mimics the inflections of the model curve and supports the hypothesis of slip modulated by water loading (Fig. 9.31A).

The Teton normal fault borders the eastern flank of the Teton Range in Wyoming (Byrd *et al.*, 1994). During the last glaciation, an ice cap up to 1 km thick inundated the highlands of Yellowstone to the north of the Tetons (Fig. 9.31B), while alpine glaciers expanded within the Tetons themselves (Foster *et al.*, 2010; Hampel *et al.*, 2007). Modeling predicts a deceleration of slip rates as the ice loads grew, and a rapid acceleration when the ice loads disappeared. Notably, the load of the Yellowstone ice cap is predicted to have a much greater effect on slip rates on the Teton Fault than do the more local, but much smaller, Teton glaciers. Given the currently known slip history of the Teton Fault, slip rates were about twice as rapid between 16–8 ka as they were between 8–0 ka: changes consistent with predicted changes as the ice disappears (Fig. 9.31B) (Hampel *et al.*, 2007).

The general match between predicted and observed slip on the Teton and Wasatch Faults is provocative and suggests that climate changes that create changes in stresses on faults can modulate their slip rates. A more convincing test of this proposed climate–tectonic linkage, however, awaits the development of slip histories that extend through an entire glacial or lake cycle and show rate changes consistent with a time-calibrated loading–unloading history.

Catch and release: seamounts and forearcs

Earlier we described the challenge of discriminating among different forearc behaviors when thickened crust, such as that represented by a seamount, is rafted into a subduction zone and collides with the forearc (Fig. 9.3). Contrasting uplift–subsidence scenarios are proposed depending on whether compression dominates as a seamount gets pinned against the front of the forearc, thereby inducing widespread and rapid uplift, or whether displacement dominates as a seamount slides under the forearc, thereby

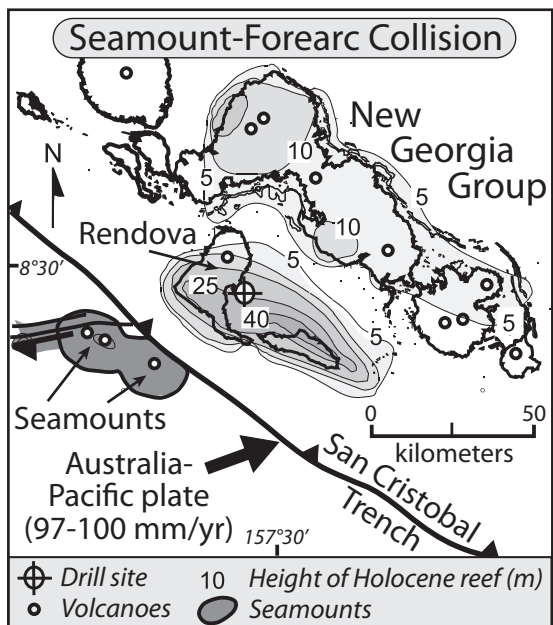


Fig. 9.32 Seamount–forearc collision in the tropical Pacific.

The New Georgia group of forearc islands sit above the rapidly converging Australia–Pacific subduction zone. Contours of Holocene reef heights indicate the pattern of recent uplift. Seamounts impinging on the subduction zone, volcanic centers, and the drill hole on Rendova island are shown. Modified after Taylor *et al.* (2005).

causing a progressive, more localized wave of uplift. Tropical coastal regions can provide fertile sites for testing these competing models, because the general history of sea-level change (both magnitude and age) is well known (Figs 2.5 and 9.4) and many coral-rich marine terraces can be dated. With these data, local terrace elevations and ages can be compared with the sea-level curve to deduce patterns and rates of uplift and subsidence.

Recent studies in the tropical Pacific have illuminated rich histories of rapid uplift and subsidence (Taylor *et al.*, 2005). In the New Georgia group (islands on the forearc of the Pacific Plate where the Australia Plate under-thrusts at a rate of ~100 mm/yr), several adjacent seamounts have entered into the subduction zone (Fig. 9.32). Holocene terraces have been differentially uplifted as much as 40 m above sea level, and they provide unambiguous evidence

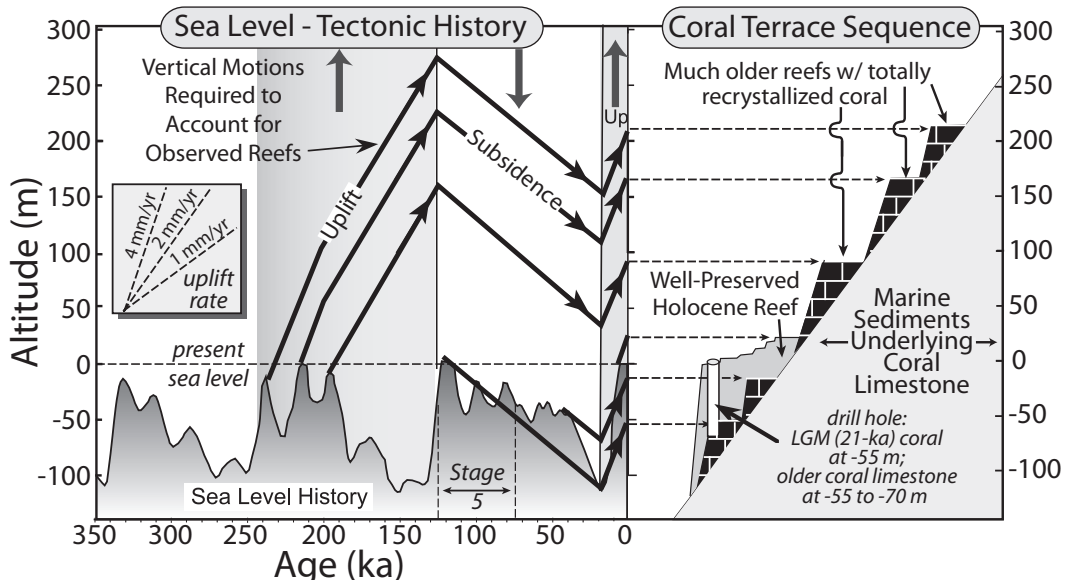


Fig. 9.33 Coral terrace sequence on the New Georgia group forearc and inferred tectonic history.

(Right) Uplifted Holocene reefs on Rendoza island (Fig. 9.32) are spatially bracketed by much older, recrystallized reefs. Drill hole shows Last Glacial Maximum (LGM) corals at -55 m, indicating ~65 m of uplift since 20 ka. No Marine Isotope Stage 5 terraces are recognized above sea level. (Left) Correlation (black lines) of sea-level history with observed and dated terraces defines abrupt changes in uplift and subsidence over the past 250 kyr. Modified after Taylor *et al.* (2005).

for recent uplift at rates as high as 6 mm/yr (Taylor *et al.*, 2005). Similarly, drill-hole data reveal that Marine Isotope Stage 2 terrace deposits that were formed at a depth of ~120 m are currently only at -55 m (Fig. 9.33) and define an average uplift rate of ~3 mm/yr since 20 ka. But these rates have not been sustained for long: no Marine Isotope Stage 5 terraces are currently exposed above sea level, and terraces immediately above the Holocene terraces are completely recrystallized, indicating their overall antiquity (Fig. 9.33). These observations provide persuasive evidence for multiple and abrupt changes in forearc uplift and subsidence over the past 20–300 kyr. Taylor *et al.* (2005) argue that these changes could not be induced by a displacement (underthrusting) mechanism (Fig. 9.3). For example, over the past 40 kyr, as rapid subsidence was replaced by rapid uplift, an impinging seamount would have advanced only a few kilometers, not enough to cause such an abrupt transition. Instead, Taylor *et al.* (2005) suggest that subsidence–uplift history is consistent with impinging seamounts that jam up the subduction

process, cause temporary locking of the upper parts of the subduction zone, and drive elastic-like compression of the nearby forearc. Seismic rupturing of the seamount is speculated to cause collapse of the forearc and rapid subsidence, as is seen in the New Georgia islands. This striking example of abruptly changing patterns of uplift highlights the potent insights that can be gleaned at intermediate time scales when well-dated geomorphic markers with known initial positions can be tracked as they deform.

Summary

Tectonic deformation and interactions with surface processes over intervals of hundreds of thousands of years produce the landscapes that we see today in many tectonically active areas. At vertical uplift rates of about 1 mm/yr and horizontal displacement rates of about 1 cm/yr, hundreds of meters of uplift and several kilometers of lateral displacement occur over these “intermediate” time spans. In combination with climatic

and lithologic variations, such movements exert a fundamental control on landscape development.

Given the slope dependence of many surface processes and the sensitivity of fluvial systems to small variations in surface gradients, geomorphic responses to specific tectonic perturbations are commonly predictable. At intermediate time scales, powerful insights are obtainable when the growth of structures can be quantified. Not only does this quantification reveal mean rates of deformation and structural propagation, but it also provides a reliable context for interpreting geomorphic responses to deformation and testing predictions concerning those responses.

Numerous difficulties, however, can thwart successful landscape analysis at intermediate time scales. Determination of tectonic rates typically depends on dating of displaced geomorphic surfaces. In many geomorphic settings, dating of surfaces that exceed the range of radiocarbon dating (>40 kyr) is difficult or impossible. Soil chronologies, uranium-series dates, cosmogenic exposure ages, or luminescence ages can sometimes bridge the gap between radiocarbon and argon–argon dating. Because each of these dating approaches may lack accuracy, reliability is improved by (i) the use of several techniques in conjunction with each other whenever possible, (ii) a focus on settings in which redundant ages can be determined for the same surface, or (iii) use of sites for which multiple rate calculations can be made from a succession of offset markers.

In tectonically active coastal settings, ages of terraces are often inferred through correlation with a dated sea-level curve. Numerous uncertainties still exist in this curve with respect to both the magnitude of past sea-level variations and the actual timing of those changes. The interval prior to the last interglaciation (>130 ka) has only been partially calibrated. To the extent that the reliability of the sea-level curve and resulting correlations can be enhanced, the accuracy of deformation rates in coastal domains will improve.

The timing of geomorphic responses to climate variations in terrestrial settings is even less well understood than those along the coast. Development of some geomorphic markers,

such as fluvial terraces, have both direct and indirect climate controls. For example, even if climatic conditions are conducive to terrace building, if insufficient sediment is available for transport within the upstream drainage, aggradation will not occur. Nonetheless, geomorphic markers provide a critical basis for gauging deformational and denudational processes within many landscapes. Therefore, understanding of the character and rates of response of markers to climatic changes, as well as the temporal lags in those responses and the potential impact of autocyclic processes, is of paramount importance in reconstructing tectonic and geomorphic histories at intermediate time scales.

The punctuated production of geomorphic markers by climatic variations provides a means both to delineate changes in tectonic rates and deformation patterns through time, and to create a robust framework in which to examine landscape evolution. At intermediate time scales, accumulated displacements can be sufficiently large to allow incisive testing of conceptual models for fault and fold propagation through time, fault linkage, steadiness of fault-slip rates, and stick-slip behavior in subduction zones at multi-millennial time scales. Where rates can be shown to change, transient landscapes can be used to explore how the surface responds to changing boundary conditions.

Individual folds commonly grow over an interval of a few hundred thousand years in tectonically active settings. During this period, stream patterns and preserved surfaces commonly provide unambiguous information on the amount and geometry of deformation. If fold growth were to persist at rates of 1 mm/yr for a million years, 1 km of displacement would occur. In most cases, structural relief of this magnitude would cause erosion to obliterate all but the most persistent geomorphic markers, such that the details of fold evolution would be difficult to reconstruct from geomorphology alone. It is at these longer time scales, however, that mountain ranges develop and orogens evolve. In the succeeding chapter, we examine landscapes that represent an integration of geomorphic and tectonic processes at time scales of a million years or more.